

Design and Validation of an Octopus-Inspired Suction Cup with High-Resolution Tactile Sensing for Soft Robotic Arms

a Master Thesis written by

Stein van Veggel

to obtain the degree of Master of Science at the
Delft University of Technology, to be defended publicly on
Wednesday 25th of October, 2023 at 10:30 AM.

Student Number:	4562100	
Project Duration:	September 2022 - October 2023	
Thesis Committee:	Dr. M. Wiertelwski,	TU Delft Cognitive Robotics, Chair
	Dr. Ir. Doubrovski, E.L.	TU Delft Sustainable Design Engineering, Chair
	Kooijman, A.	TU Delft, Mentor
	Dr. Scharff, R.B.N.	Hong Kong University of Science and Technology, External Mentor
	Ir. Sakes, A.	TU Delft, External Committee member



Faculty of Mechanical, Maritime and Materials Engineering | Department of Cognitive Robotics
Faculty of Industrial Design Engineering | Department of Sustainable Design Engineering
Delft University of Technology, the Netherlands

Design and Validation of an Octopus-Inspired Suction Cup with High-Resolution Tactile Sensing for Soft Robotic Arms

Stein van Veggel

Abstract

In the field of soft robotics, rigid joints and links are replaced by soft, deformable elements. This causes soft continuum robot arms to excel in unpredictable environments, but to face challenges during control and shape reconstruction. The sensing ability present in octopus suckers provides inspiration for solutions. Octopuses employ their suckers not only to strengthen their grasp but also as tactile sensors to control the shape and position of their soft arms. This has motivated researchers to integrate artificial sensorized suckers in soft continuum robot arms. Although various sensorized suckers have already been developed, their employed sensing methods tend to be low in resolution and are often poorly embedded into the overall sucker architecture. In this work, these limits are overcome by presenting an octopus-inspired suction cup with integrated high-resolution tactile sensing abilities. This is achieved by utilizing the Chromatouch Principle, which relies on embedding colored markers in the suction cup membrane. Tracking these markers with a camera produced tactile images containing useful information about forces, deformations and interactions with objects. Fabrication with multi-material additive manufacturing enabled direct integration of these markers into the suction cup membranes. We demonstrated the design's basic functionality by conducting pull-off and pickup tests. The design exhibited a normal pull-off force of 9.53 N and a shear pull-off force of 5.28 N. It was also able to successfully pick up both flat and curved objects. The sensing ability was showcased by training a Convolutional Neural Network to learn the relationship between the camera images and the orientation of the suction cup with respect to a touching substrate. Using a spherical coordinate system, the orientation could be predicted with an error of less than 2 degrees for latitude and less than 9 degrees for longitude. This performance was validated by using the trained network to successfully correct the orientation when picking up objects under an angle. For a single suction cup, this ability can be utilized to correct the orientation and achieve perpendicular contact with an object, crucial for achieving a seal. On a larger scale, the integration of multiple suction cups in soft continuum robot arms has the potential to form a representation of the arm shape as a whole. It can thereby contribute to overcoming the control challenges faced in the field of soft robotics.

I. INTRODUCTION

Traditional robotic approaches are characterized by high precision, speed, and reliability. However, they come with a fundamental limitation – rigidity. These robots, equipped with rigid joints and links, have a finite number of degrees of freedom, typically only six. In the field of soft robotics, these rigid joints and links are replaced by soft, deformable elements, providing soft robots with an infinite number of degrees of freedom. This inherent flexibility enables them to easily adapt their shape in unpredictable and unstructured environments.

However, soft robotic approaches also come with two important challenges. First, soft-bodied robots are characterized by low force outputs and slow response times due to their compliance [1]. The second challenge addresses the control difficulty. The flexibility of soft robots comes with the need for precise control over their position and shape [2]. While conventional robot control approaches rely on shape reconstruction by using inputs from linear and rotary sensors, the high number of degrees of freedom in the shape of soft robots makes this strategy difficult, which thereby complicates control.

To address these challenges, researchers have turned to nature for inspiration, particularly studying the manipulation and control strategies employed by octopuses. Octopuses employ their suckers not only to strengthen their grasp but also as tactile sensors to control the shape and position of their soft arms (Appendix VIII-A). This motivates the

integration of designing artificial sensorized suction cups for soft continuum robot arms, in order to overcome the force- and control-challenge in soft robotics.

This work encompasses the design and validation of such a sensorized suction cup. A vision-based approach was chosen as the sensing-method, relying on ‘tactile’ images captured by a camera that tracks the suction cup membranes. By embedding a pattern of colored markers in these membranes, the captured images provide high resolution sensing data, rich in information about the suction cup’s deformation. Machine learning approaches decode the information from the images, enabling to use the information for effective control strategies. Figure 1 shows the final design.

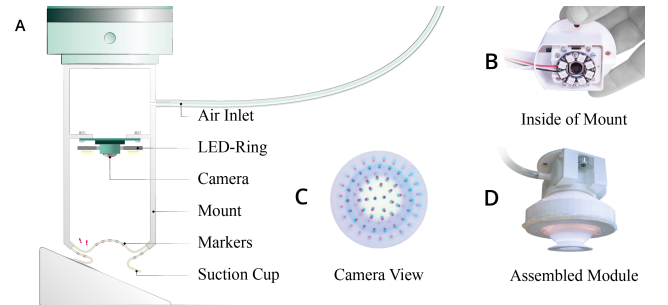


Fig. 1: (A) Final design concept. (B) Inside of the mount, accommodating a camera and a LED-ring. (C) Camera view (D) Assembled suction cup in the mount.

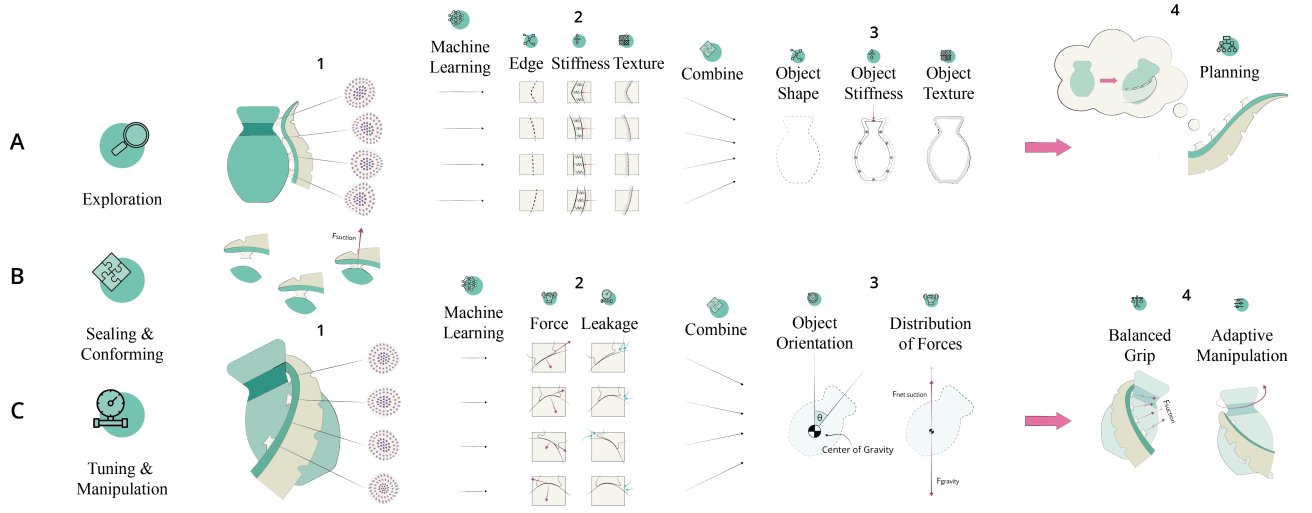


Fig. 2: Envisioned future use of the sensorized suction cup when integrating multiple in a soft continuum robot arm. The scenario is divided into three phases. **(A)** the 'exploration phase', where tactile images are used to form a representation of the external environment, and construct a planning for approach, **(B)** The 'sealing & conforming phase', where the suction cups are placed onto the substrate and attachment forces are formed through negative pressure, and **(C)** the 'tuning & manipulation phase', where tactile images are used to obtain information about leakage and force distributions in order to effectively interact with the object.

To illustrate the potential use of this suction cup in a soft continuum robot arm, consider the scenario shown in Figure 2. It encompasses three phases. First, the 'exploration phase' (Figure 2A), where the tactile images are decoded to extract information about the shape, stiffness, and texture properties of objects. By combining their data, a representation of the object and the arm's own shape can be reconstructed, enabling it to formulate an appropriate approach. In the second phase, the 'sealing & conforming phase' (Figure 2B), the suction cups establish a seal on the object, using negative pressure to create an attachment force. Tactile images are now primarily used to sense contact and ensure a seal. The third phase, the 'tuning & manipulation phase' (Figure 2C), involves using the images to detect leakage and analyze force distributions. This helps to retrieve object properties such as weight, orientation, and center of gravity. It aids in fine-tuning the attachment force, enabling a balanced grip and adaptive object manipulation.

This research narrows the scope to the orientation of a single suction cup with respect to an object boundary. This is motivated by the key challenge to achieve perpendicular contact between the suction cup and the substrate, which is necessary for a proper seal and attachment force. This simplified part of the scenario is shown in Figure 3. The objective is to prove that integration of a vision-based sensing approach in a suction cup, combined with a machine-learning based approach for decoding the tactile images, enables to retrieve its orientation with respect to an angled substrate. Using this information to adapt this orientation will enable to obtain a proper seal between the substrate and the suction cup.

This work is structured as follows. First, the design and manufacturing process of the suction cup is explained. Then, two experiments are conducted. The first experiment addresses the basic functionalities a suction cup should have by conducting pull-off tests and object pickup tests. In these tests, it is also shown that useful tactile images are obtained during these tasks. The second experiment focuses specifically on the sensing ability, and concentrates on obtaining a perpendicular seal in the absence of external visual cues. It addresses the recognition of the suction cup's orientation with respect to angled substrates. For this, a Convolutional Neural Network will be trained to learn the relationship between images taken during tilted contact with a substrate, and the orientation of the suction cup relative to this substrate. This final experiment will answer the following research question: "Can a Trained Convolutional Neural Network Accurately Predict the Orientation of a Suction Cup Relative to a Substrate, based on Tactile Images Captured by Integration of Vision-based Tactile Sensing, and thereby

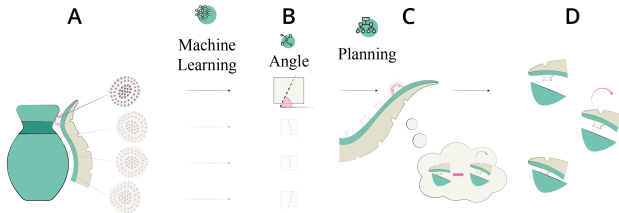


Fig. 3: Simplified version of the scenario, where the scope is narrowed to a single suction cup that uses its tactile images **(A)** to recognize its orientation with respect to an tilted substrate **(B)**. The information is used to correct the orientation of the soft robot arm **(C)** to obtain perpendicular a perpendicular contact and seal with the substrate **(D)**.

II. RELATED WORK

A. Artificial Suction Cups

Van Veggel et al. (Appendix VIII-A) investigated the state of the art in soft robotic suction cups. Considering integration of tactile sensing in artificial suckers, several designs exist. Huh et al. [3] measured the differential pressure between four inner chambers in their suction cup to obtain information about surface curvature, proximity, and texture. Sareh et al. [4] used a fiber optic head in the sucker to measure proximity and tactile information, for use in motion planning and measuring substrate stiffnesses. Frey et al. [5] used a micro-LIDAR optical sensor next to the suction cup to measure proximity, and activated the membrane when approaching an object. Lee et al. [6] spray-coated four strain sensors on the suction cup’s outer wall. They used machine learning algorithms to successfully estimate the object’s weight and center of gravity from these input channels. Shahabi et al. [7] integrated four microfluidic strain sensors into a silicone suction cup. By using the sensor outputs in machine learning algorithms, they were able to estimate angles, directions, stiffnesses, and inclinations of substrates. For a more comprehensive overview, the reader can refer to the literature research work of Van Veggel et al. (Appendix VIII-A).

Several limitations exist in the current designs. The spatial distribution of sensing channels is often limited, usually reaching only up to four channels, which limits the spatial sensing resolution. Also, the degree of integration into the suction cup’s architecture is low. Many implementations rely on external sensors that increase the size of the module, or employ rigid sensors that interfere with the suction cup’s deformability, thereby limiting attachment to irregular surfaces. Additionally, the sensed information is rarely used for control. In conclusion, the state-of-the-art sensorized suction cup designs have not yet achieved the desired maturity level to integrate them into a soft continuum arm and address the proposed control challenges. This work aims to bridge this gap by embedding a vision-based tactile sensing principle into a suction cup. These types of sensing technologies usually employ a camera to track the displacement of markers embedded in a soft elastomer membrane [8]. Advantages of these methods are their high spatial resolution and minimum wiring requirements compared to other sensing technologies. While several types of vision-based technologies exist, this work employs the ChromaTouch Principle [8], [9], [10], [11].

B. The Chromatouch Principle

The reason for choosing the Chromatouch principle over other technologies is its ability to deduct both lateral and normal deformation of the elastomer membrane, forming

a three dimensional representation of the deformation field. This puts it in a favorable position against other vision-based technologies which are often solely able to track the lateral membrane deformation. The principle works by having each marker consist of two superimposed color filters (Figure 4). The color of the partially translucent magenta markers on the inner layer is mixed with the opaque cyan markers on the outer layer. As a result, the centroids of both layers can be tracked simultaneously, even when the color filters overlap, resulting in a higher number of markers and a better spatial resolution. Detection of the centroid displacement of each marker is used to determine lateral deformation of the membrane, while normal displacement is tracked by subtractive color mixing. A change in normal force on the membrane results in a change of distance between the two color filters, which alters the ratio of cyan to magenta in the marker sub-image. This variation in hue is used to track the normal deformation.

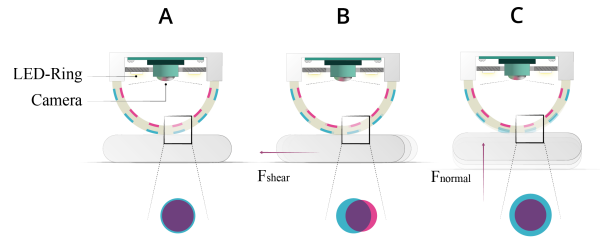


Fig. 4: Explanation of the ChromaTouch Principle. (A) Neutral state, where the markers fully overlap and the marker sub-image appears purple. (B) Application of a shear force, where the cyan color-filter, located further from the camera, tangentially moves with a larger amplitude compared to the closer magenta color-filter. This changes the relative distance between the two and causes the image to appear as a superposition of two circles with their intersection subjected to subtractive color mixing. (C) Application of a normal force, where the compression of the elastomer causes the cyan filter to occupy a larger portion of the sub-image

The principle is visualized in Figure 4. In the initial state, the sensor remains undeformed, and the markers exhibit a consistent purple color of cyan and magenta layers (Figure 4A). When shear forces are applied, the closer cyan layer tangentially moves with a larger amplitude compared to the magenta layer due to the elastic properties of the membrane. Consequently, the marker sub-image shows the superposition of two circles, with their intersection undergoing subtractive mixing and appearing purple (Figure 4B). The application of a normal force compresses the elastomer, decreasing the distance between the two color-filters and causing the cyan layer to occupy a larger portion of the sub-image (Figure 4C).

To date, the ChromaTouch Principle has been demonstrated in a flat elastomer membrane [9] and hemispherical robot fingertips [8], [10], [11]. The first versions were still manufactured by multiple stages of silicon casting [9], [8] but the more recent versions employed multi-material additive manufacturing. Also, while previous versions were still calibrated by employing ground-truth models such

as Hertzian Contact Theory [9], [8], [10], Boonstra [11] has proven the use of the ChromaTouch images in a Convolutional Neural Network. He demonstrated the ability of these networks to learn the relationship between tactile images and the safety margin, and showed its potential use in mimicking human grasp control.

III. DESIGN & MANUFACTURING

A. Design Process

Although this work's main focus is to recognize and correct the orientation error (Figure 3), the suction cup was designed with the full scenario in mind (Figure 2). The design process can be found in Appendix I, which includes formulating design requirements originating from the scenario (Appendix I-A), creating a morphological map (Appendix I-B), developing three concepts, (Appendix I-C) and the concept selection (Appendix I-D).

This work's design adopted a fluidic actuation method, relying on an air pump and utilizing a membrane between the internal and external medium. More information about this choice can be found in Appendix II-A. The Octopus *Vulgaris* sucker served as an inspiration source for the sucker architecture (Appendix II-B). Similar to the octopus sucker, the suction cup consists of two chambers, the infundibulum and the acetabulum, which are connected through an orifice (Figure 5A). The infundibulum is responsible for conforming and sealing to a broad range of substrates, while the acetabulum produces the volume change required for the pressure decrease.

The design contains two layers of markers (Figure 5). The first marker layer is embedded in the acetabular roof (upper membrane) and is directly visible to the camera. The second layer is located in the acetabular wall (lower membrane) and is indirectly visible through the edge of the transparent acetabular roof. It is expected that this type of marker architecture provides an information-rich type of image data. Elaborated examples can be found in Appendix II-D. In addition to this, a sample test to assess the visibility of the second layer of markers under different layouts can be found in Appendix II-C.

B. Adhesion Process

The proposed design incorporates the acetabular roof (top membrane) in two states. The first state corresponds to the 'exploration phase' of the scenario (Figure 2A), where the membrane is inflated (Figure 5B2). After achieving a seal (Figure 5B3), the second state is activated, which involves retraction of the membrane by activation of vacuum pressure (Figure 5B4). This leads to a volume increase in the sealed chamber, resulting in a pressure drop and the production of an attachment force.

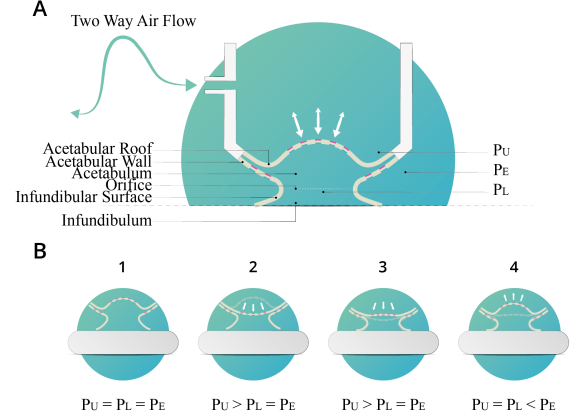


Fig. 5: (A) Annotation of pressures in locations relevant for the adhesion process. P_U : Pressure in chamber above the acetabular roof, directly connected to the fluidic circuit, P_L : Pressure in the acetabular and infundibular chamber, which becomes sealed after a tight contact with the substrate is achieved. P_E : Environmental pressure. (B) Steps of the adhesion process in the design. (B1) Approaching the substrate with the membrane in a neutral state. All pressures are equal to atmospheric pressure P_E . (B2) Activation of the pump inflates the acetabular roof, increasing P_U . P_L is still equal to P_E as no seal has yet been achieved. (B3) Pressing the suction cup against the substrate forms a seal. (B4) Activation of the vacuum decreases P_U and thereby retracts the acetabular roof, increasing the volume of the chamber between the suction cup and the substrate. As this chamber is now sealed, this creates a pressure drop in P_L .

C. Manufacturing, Post-Processing & Assembly

The suction cup was parametrically modelled in Rhino Grasshopper. This aided rapid experimenting with different geometrical parameter values. Appendix II-E describes the process of testing and selecting these values. The chosen geometry resulted in a theoretical pressure change in the suction chamber (ΔP) of 88.1 kPa and a theoretical attachment force (F_{MAX}) of 100.2 N.

Both the top and bottom parts of the suction cup were manufactured by Polyjet printing with the Stratasys J35 (Figure 6A1). This made it possible to embed the markers in both membranes without requiring extra fabrication steps, thereby minimizing the risk of defects that could cause leakages. It also enabled the inclusion of a rigid edge,

required for mounting the suction cup during the experiment. The colors of the markers were chosen from the translucent VeroVivid family. For the outer cyan layer, VeroCyan-V was used. The inner marker layers were fabricated in the more opaque VeroMagenta-V. The deformable parts were all printed in Agilus30Clear. For the rigid edge, VeroPureWhite was chosen. The support material was printed in SUP705, which is a gel-like, easily breakable material. Two other versions of the prototype that were not further included in the experiment, can be found in Appendix III.

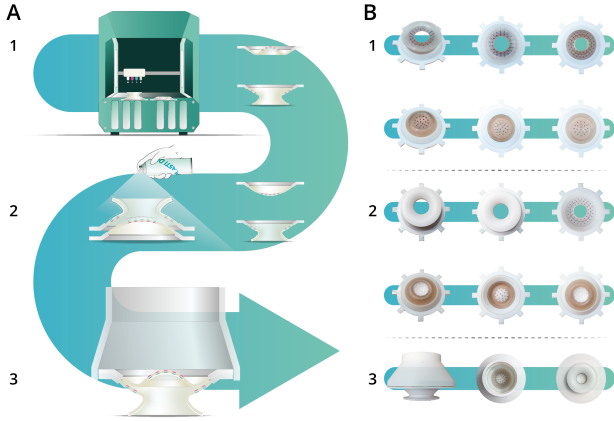


Fig. 6: (A) Manufacturing steps. (A1) Fabrication of top and bottom parts by polyjet additive manufacturing with the Stratasys J35, (A2) Spraying Plasti-Dip onto the highlighted parts, (A3) Bonding the top and bottom and attaching them to a PLA 3D-printed mount. (B) Pictures in different stages of the process. (B1) Top and bottom parts before application of Plasti-Dip and (B2) after application of Plasti-Dip. (B3) Assembled module consisting of top part, bottom part, and PLA 3D-printed mount

After the printing process, a white rubber spray-coating (Plasti-Dip ¹), was sprayed onto the parts highlighted in Figure 6A2. To conserve the transparency of the acetabular

roof's circular edge, this part was masked during the spraying process. The purpose of the Plasti-Dip layer is twofold. First and foremost, it blocks external light from outside from interfering with the tactile images. Second, it equally distributes the light throughout the chamber above the acetabular roof.

A mount was 3D printed with PLA and attached to the suction cup with a glue gun (Figure 6A3). This mount was used for attachment to the UR5 Robot arm during the experiment and the housing of the electronic components (Figure 7). These components encompassed an Adafruit Neopixel 8-bit LED ring for the internal lighting, a wide-lens Raspberry Pi Camera Module V3 for capturing the tactile images, and a BMP280 barometric pressure sensor for recording the internal pressure. The mount has two inlets, one for the pneumatic channel and one for the wiring of the barometric sensor, camera and LED ring. The distance between the end of the mount and the upper part of the suction cup is 50 mm, which was found to be the minimal focus distance of the camera module. The TinkerMinds programmable air device was attached to the pneumatic inlet of the mount. This device consists of an Arduino Nano, two pumps and three valves. The resulting pneumatic circuit was able to apply both vacuum and compression on several power levels. The camera module and the barometric pressure sensor were connected to a Raspberry Pi 3. In order to control all hardware components from the Raspberry Pi environment, a serial connection was made between the Arduino and the Pi by plugging the Arduino USB Cable into the Raspberry Pi. This enabled the Raspberry Pi to send serial commands to the Arduino. Finally, the mount was attached to the end-effector of the UR5. For force measurements, an acrylic plate of dimensions 100 x 100 mm, serving as the substrate, was attached to the Wittenstein HEX 32 6-Axis Force/Torque Sensor Kit. The setup is schematically shown in Figure 7A, together with the real-life setup in Figure 7B.

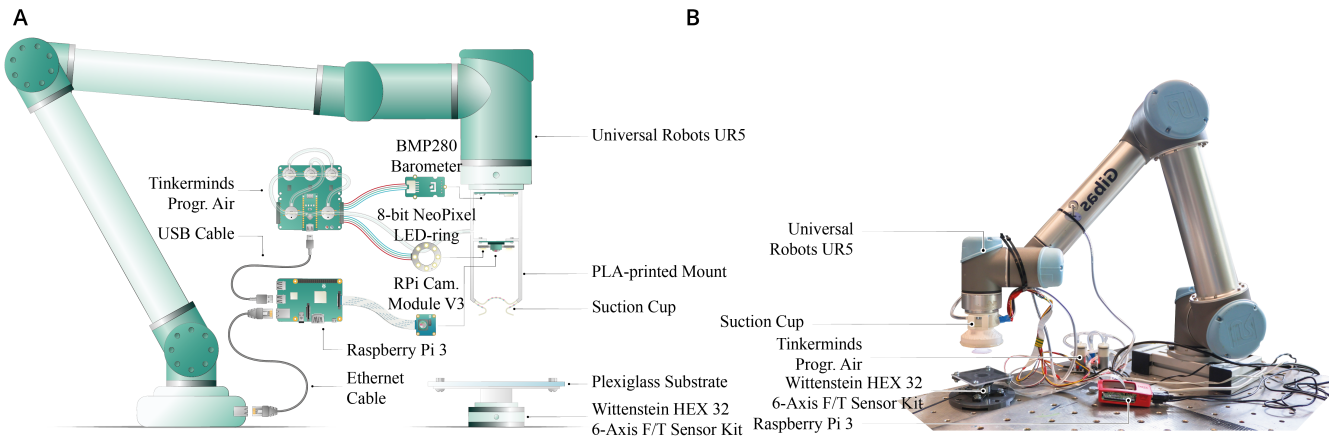


Fig. 7: (A) Schematic view of the test setup. (B) Annotated picture of the test setup

¹Plasti Dip Nederland. "Plasti dip spray mat wit". URL: <https://www.plasti-dip.nl/shop/plasti-dip-spray-mat-wit/>. Accessed: 15-08-2023

IV. EXPERIMENTAL METHOD

A. Basic Functionality

As described in the introduction (Section I), two experiments were conducted. The first experiment focused on the evaluation of the suction cup's basic functionalities. This assessment included two pull-off tests to evaluate performance under normal and shear forces on a flat surface, as well as pickup tests involving three different objects. During all tests, tactile images were captured at every step, which were assessed on their suitability for control-related purposes.

1) Normal pull-off Strength:

The objective of the normal pull-off tests is to determine the indentation and preload that correspond to the highest normal pull-off force. As normal pull-off force is a commonly used metric for the evaluation of artificial suction cups (Appendix VIII-A), measuring it will facilitate an objective performance comparison to other state-of-the-art designs. The preload and pull-off force was measured at six different indentation levels, ranging from 1.0 mm to 3.5 mm in steps of 0.5 mm. An indentation of 0 mm is defined as the point at which the suction cup exactly touches the acrylic plate but no deformation has yet taken place. The experimental procedure used the setup depicted in Figure 7 and was executed in line with the adhesion process described in Figure 5. During every stage, force and pressure data was collected at 100 Hz and tactile images were obtained at 30 fps. The full process consisted of the following steps:

- 1) The pump was activated at positive pressure, causing inflation of the acetabular roof.
- 2) By translating the end-effector of the robot arm in the negative z-direction, the suction cup was moved downwards until it reached the determined indentation. This produced a preload force on the substrate.
- 3) The pump was activated at vacuum pressure, resulting in retraction of the acetabular roof. The volume increase of the sealed chamber between the suction cup and the substrate generated a pressure drop and led to an attachment force.
- 4) The robot arm was translated in the positive z-direction at an acceleration and velocity of 0.01 m/s and 0.01 m/s² respectively, resulting in the suction cup being pulled off the substrate.

Data post-processing required time-synchronizing the force- with the pressure- and image data, as they were collected on different devices. This synchronization was based on the moment of indentation, which corresponds to the minimal (negative) force in the z-direction on the substrate and the maximum (positive) pressure in the chamber above the acetabular roof. This is because the indentation caused a slight upward movement of the acetabular roof, resulting in

a small pressure peak. The normal pull-off force was then defined as the maximum of the z-component in the force data sequence, while the preload force was defined as the minimum. A video of the normal pull-off test can be found in Appendix IX-A.

2) Shear pull-off Strength:

To proceed with the shear pull-off test, the indentation corresponding to the highest normal pull-off force was selected. This test followed a similar procedure to the normal pull-off test, with one key distinction. Instead of translating the robot arm in the z-direction after activation of the vacuum, the arm was now translated in the x-direction, generating a shear pull-off force. A video of the shear pull-off test can be found in Appendix IX-A.

3) Object Pickup Tests:

The pickup tests also followed the same steps as the normal pull-off experiment, with one distinction. Instead of using the velocity and acceleration of 0.01 m/s and 0.01 m/s² in step 4, these values were now increased by a factor 5 to speed up the pickup of the object. Three objects were used. First, an aluminum block weighing 12.0 g and dimensions 55 x 40 x 20 mm (l x b x h). This object was lifted with the center of gravity aligned with the central axis of the suction cup. Second, an elongated aluminum profile weighing 33.0 g and dimensions 150 x 40 x 20 mm. This object was lifted with its center of gravity 50 mm from the suction cup central axis. Lastly, to assess the adaptability to curved objects, an aluminum cylinder weighing 17.5 g with a 16 mm radius and length of 75 mm was picked up. During all pickup tests, pressure data was gathered at 100 Hz. Videos of all three pickup tests can be found in Appendix IX-B.

B. Orientation Recognition

The second experiment addressed the ability to recognize the orientation with respect to tilted substrates. However, to automate and simplify the data collection process, a flat substrate rather than a tilted one was used. The tilted contact was then instead obtained by using the robot arm to put the suction cup in a randomized orientation before indenting it on the substrate and taking an image. A Convolutional Neural Network was trained to learn the relationship between these images and the orientation of the suction cup relative to the substrate.

1) Data Collection Method:

The first phase of this experiment involved the collection of orientation-labelled tactile images. A quasi-static approach was adopted, leaving a sufficient amount of time between capturing each image. This ensured that damping and other

dynamic effects of the visco-elastic Agilus30Clear did not introduce unwanted variations in the tactile images. Also, to eliminate variation introduced by camera focus, the lens distance was set to the minimal value of 50 mm and autofocus was disabled. The resolution of the captured images was 1170 x 1170 pixels. Figure 8A explains how the orientations were defined. A spherical coordinate system was adopted where the center of rotation was located at the intersection of the suction cup's central axis and the circular area defining the edge of the infundibulum (Figure 8)A1). After defining a randomized target orientation (Figure 8)A2) in a latitude domain between 0° and 20° , and a longitude domain between 180° and -180° (Figure 8)A3), the suction cup was rotated into the target orientation (Figure 8)A4). With the goal of making the Convolutional Neural Network able to generalize its predictions over varying indentation levels, a randomized indentation between 3.0 mm and 4.0 mm, with steps of 0.2 mm in between, was generated. Figure 8B1 shows that the zero-level was defined as the outer edge of the infundibulum slightly touching the substrate. The suction cup was then translated in the negative z-direction of the world coordinate system until the desired indentation was reached (Figure 8B2). An explanation video, showing multiple randomized orientations and indentations, can be found in Appendix IX-C.

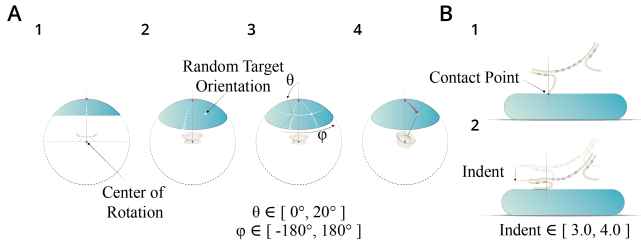


Fig. 8: (A) Definition of orientation in a spherical coordinate system. (A1) The center of rotation is defined as the intersection of the suction cup's central axis and the circular area defining the infundibulum edge. (A2-A3) A random target orientation is generated in a latitude domain between 0° and 20° , and a longitude domain between 180° and -180° . (A4) The suction cup is rotated in the target orientation. (B) Definition of the tilted indentation on the substrate. (B1) Achieving initial contact with the infundibulum edge. (B2) Moving the suction cup in the world negative z-direction until the desired indentation is reached

Having adopted the system in Figure 8 to define the orientation and indentations, the following steps were executed for the data collection process (Figure 9):

- 1) The robot arm started from a neutral position, with the lowest part of the suction cup positioned 30 mm above the substrate (Figure 9A).
- 2) The pump was activated at positive pressure, causing inflation of the acetabular roof (Figure 9B).

- 3) After introducing a waiting period of 2.0 s to allow for damping of vibrations in the membrane, the first image was captured (Figure 9C).
- 4) The robot arm rotated the suction cup until it reached the desired orientation (Figure 9D).
- 5) The robot arm translated into the negative z-direction until it reached the desired indentation (Figure 9E).
- 6) After another waiting period of 2.0 s, the second image was captured (Figure 9F).

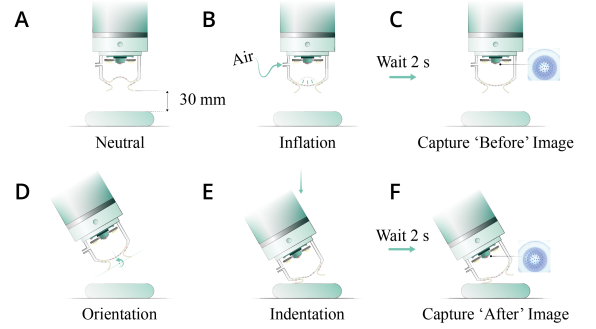


Fig. 9: Steps required for collecting the data. (A) Neutral position with the lowest part of the suction cup located 30 mm above the substrate. (B) Inflation of the acetabular roof. (C) After a waiting period of 2.0 s, the 'before' image was captured. (D) The robot arm rotated the suction cup until it reached the desired orientation. (E) The robot arm moved in the negative z-direction until the desired indentation was reached. (F) After a waiting period of 2.0 s, the 'after' image was captured.

2) Image Post-processing:

The second phase of the experiment involved post-processing the tactile images before feeding them to a Convolutional Neural Network as training data. To ensure solely capturing relevant deformations introduced by the angled indentation and eliminate unnecessary background information, the two images were processed as a single difference image. Python OpenCV's subtract algorithm was employed for this operation. It is important to note that the OpenCV subtract algorithm preserves negative pixel outputs, resulting in a lossless difference calculation [12]. The total sequence of post-processing operations is displayed in Figure 10. After saving the difference (Figure 10A), the circle containing only the marker image was cropped out and the image is downsampled to 100 x 100 pixels to decrease the network's training times (Figure 10B). Finally, the downsampled difference image was saved and labelled with the corresponding orientation and indentation values (Figure 10C). In total, 5528 labelled difference images were collected. An explanation video of the data collection process in combination with post-processing operations, can be found in Appendix IX-C.

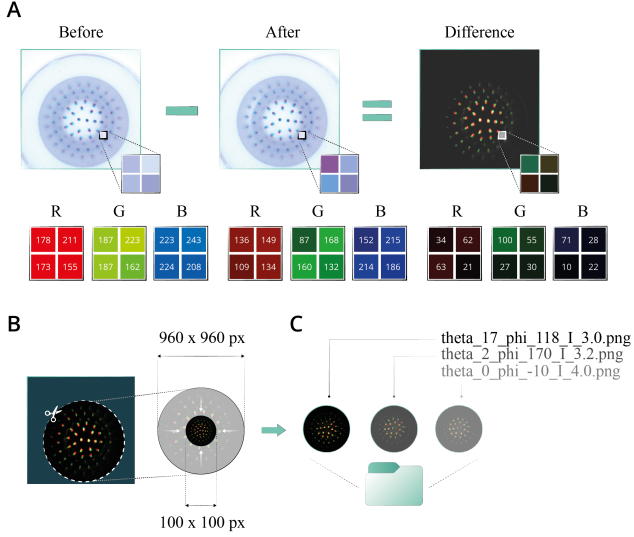


Fig. 10: Image post-processing sequence. (A) Subtracting the RGB pixel values of the ‘after’- from the ‘before’ image, leaving only the difference. (B) Cropping out the circle containing the markers and downsampling the image to 100 x 100 pixels. (C) Saving the image with the corresponding latitude (θ), longitude (ϕ) and indentation (I) labels.

3) Network Architecture & Training:

The third phase of the experiment required defining the architecture of the Convolutional Neural Network. The input dimension of the network was set to 100 x 100 x 4, corresponding to the RGBA values of the tactile images, normalized between zero and one. Then, three sequences of convolution, each with ReLu activation, and followed by a 2 x 2 Max Pooling layer were used. The output was flattened and fed into three output nodes. These three output nodes correspond to the prediction of the latitude value, normalized between zero and one ($\tilde{\theta}$), and the sine and cosine of the longitude value ($\sin(\phi)$ and $\cos(\phi)$). This deconstruction of the longitude value was used to eliminate large prediction errors close to an entire revolution. The images were randomly divided into training, validation and test data with a ratio of 0.7, 0.15 and 0.15 respectively. The network was trained in 30 epochs with a batch size of 32, the ADAM optimizer and the MSE (Mean Square Error) loss function. More information about the Convolutional Neural Network can be found in Appendix IV. This includes a grid-search process for finding the set of hyperparameters with the smallest validation loss, (Appendix IV-A), an infographic to show the architecture with a visualization of the layer activations (Appendix IV-B) and the prediction results of several random samples from the test set (Appendix IV-C).

V. RESULTS

A. Basic Functionality

It became clear that an indentation of 2.0 mm produced the optimal pull-off force of 9.35 N, with a corresponding preload of 22.2 N (Appendix V). This was achieved by activating the fluidic circuit with a positive input pressure of 15.28 kPa, followed by a negative pressure of -15.77 kPa. Figure 11A shows the tactile images taken during relevant stages of the pull-off test, along with difference images between them to visualize the change in deformation. When using this same indentation of 2.0 mm for the shear pull-off test, the suction cup achieved a shear pull-off force of 5.28 N. Figure 11B displays the tactile images during relevant stages of the process, along with difference images between the stages to visualize the deformations. The pickup tests showed that the suction cup was able to pick up all three objects successfully. The corresponding tactile images for the relevant stages in these tests for these tests are shown in Figure 12, along with difference images between the stages to visualize the changes in deformation.

B. Orientation Recognition

For the second experiment, the Convolutional Neural Network was trained in approximately 7 minutes (14 s per epoch for 30 epochs). This resulted in a training MSE of 0.044 and a validation MSE of 0.042.

Feeding the test set of images to the network resulted in an average absolute latitude (θ) error of 1.97° (9.8%) and an absolute longitude (ϕ) error of 9.41° (2.6%). Figure 13 displays the error bars for both variables against the real latitude values. Next, the generalization behavior over the indentations was evaluated. Figure 14 displays the error bars representing the prediction error per indentation. The separate lines plotted for each individual indentation can be found in Appendix V-B.

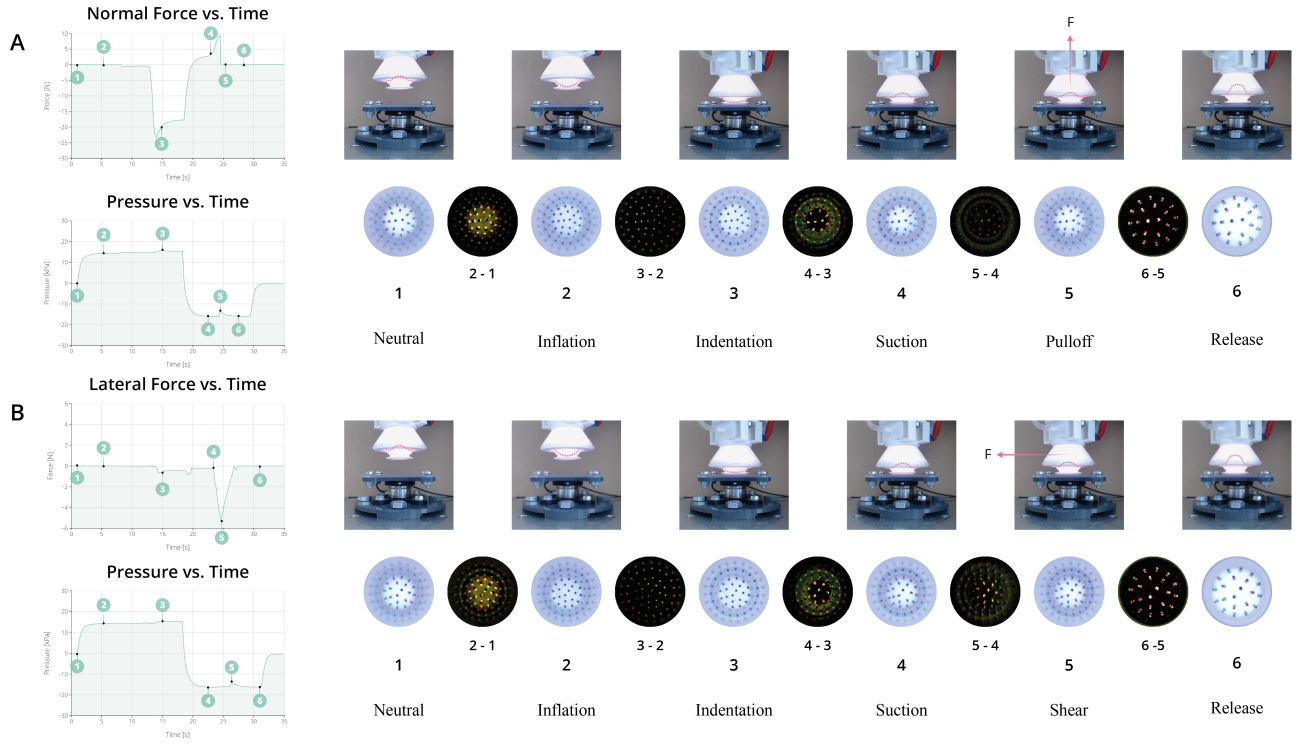


Fig. 11: **(I)** Force and **(II)** pressure plots for the **(A)** normal pull-off test and **(B)** shear pull-off test. Along with tactile images and differences images at the **(1)** neutral, **(2)** inflated, **(3)** indented, **(4)** suctioned, **(5)** pull-off and **(6)** release stage

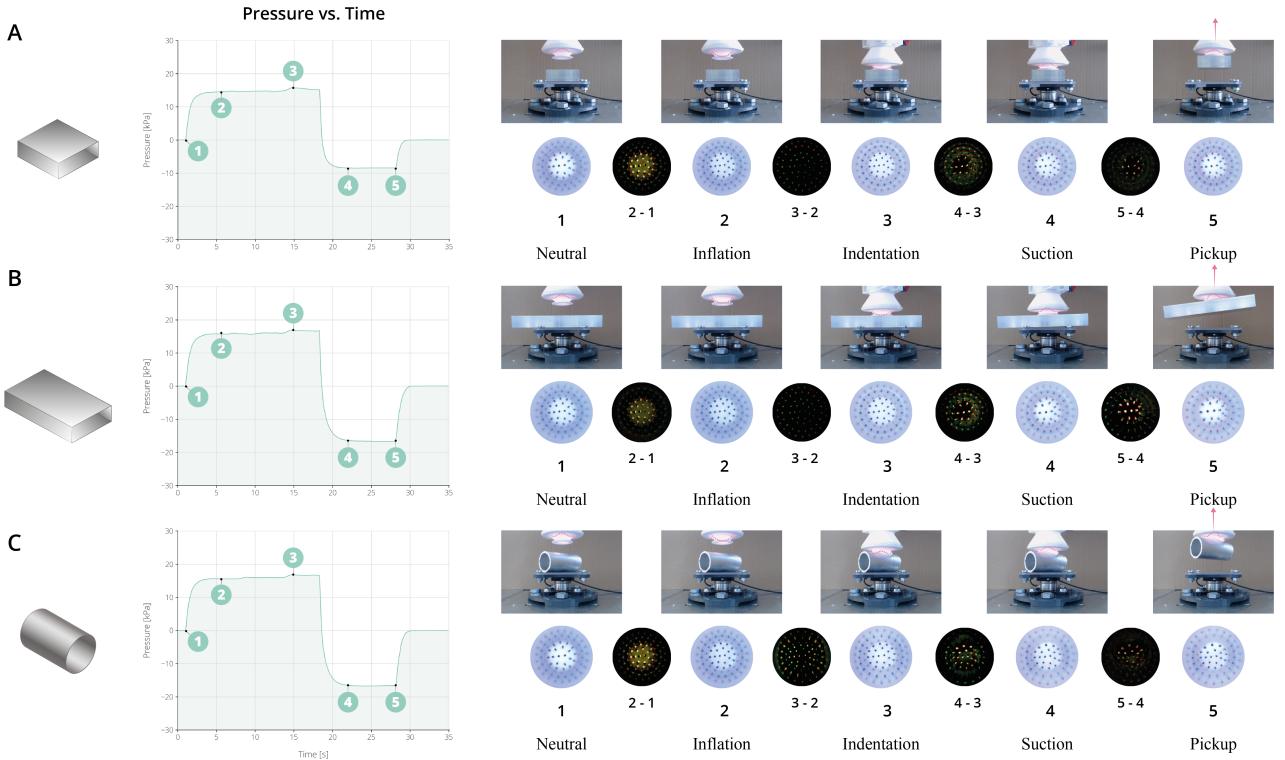


Fig. 12: Pressure plots for the pickup tests of **(A)** an aluminum block with aligned center of gravity, **(B)** beam with unaligned center of gravity and **(C)** cylinder, along with tactile images and differences images at the **(1)** neutral, **(2)** inflated, **(3)** indented, **(4)** suctioned and **(5)** pickup stage.

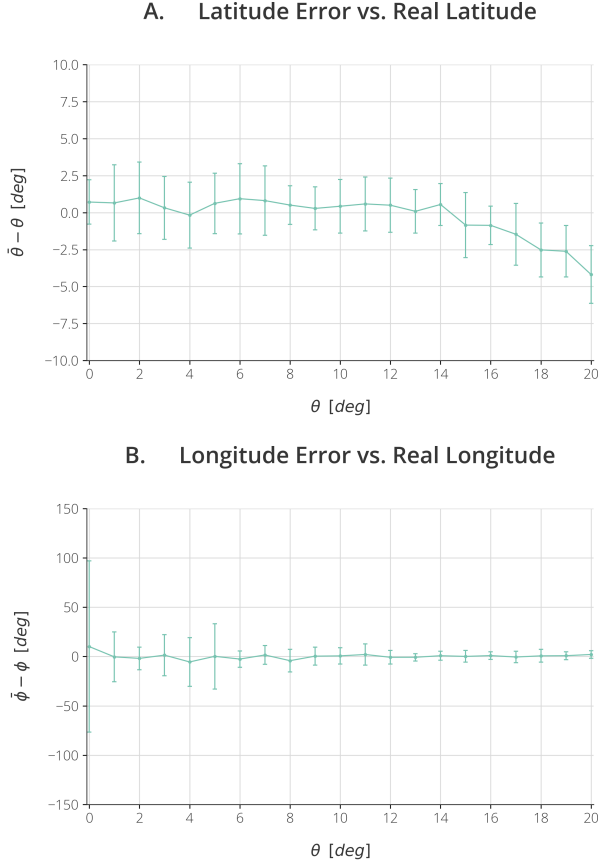


Fig. 13: Error bars for (A) latitude (θ) and (B) longitude (ϕ) prediction errors, Plotted against real latitude values.

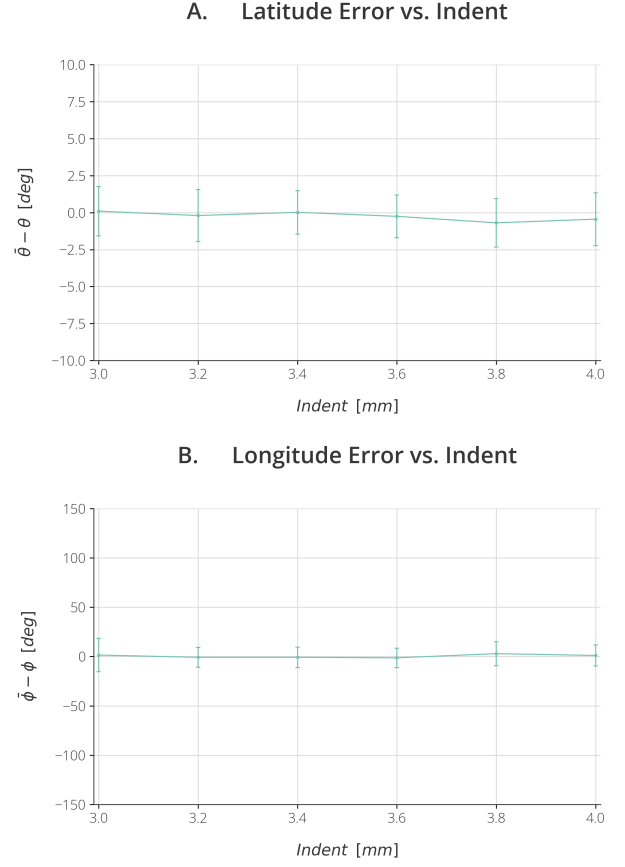


Fig. 14: Error bars displaying the (A) latitude (θ) and (B) longitude (ϕ) prediction errors over each indentation.

VI. DISCUSSION

A. Analysis of Results

As this work is primarily focused on the experimental work of this design, this section will not go into much detail about potential design improvements. Opportunities related to the design and manufacturing of the suction cup, are further elaborated in Appendix VII.

1) pull-off Test Results:

The pull-off tests demonstrated that the suction cup achieves its optimal pull-off force at an indentation of 2.0 mm, resulting in a normal pull-off force of 9.35 N with a preload of 22.2 N. Additionally, the shear pull-off force at this indentation was measured to be 5.28 N. These findings position the suction cup favorably among other state-of-the-art membrane-based fluidically actuated suction cups. As mentioned in the literature review of van Veggel et al. (Appendix VIII-A), these suction cups typically operate within a range of 5 N to 40 N for normal pull-off force.

However, it is occurring that the theoretical force of 100.2 N, calculated in Appendix II-E.1, is much greater than the actual achieved pull-off force of 9.35 N. This could be partly explained by the fact that the assumption that the pressure is equally divided over the entire infundibular surface, might be false. If it would instead be assumed that the adhesion force only occurs in the orificial area, the area decreases and the theoretical force would only be between 16 N and 18 N, which is much closer to reality. Other discrepancies could be explained by errors in geometrical assumptions of the calculation and surface roughnesses of the printed parts and Plasti-Dip coating, leading to an imperfect seal.

2) Pickup Test Results:

The pickup tests showcased the ability to grasp both flat and curved objects. Furthermore, the suction cup successfully demonstrated the ability to pick up an object with its center of gravity displaced from the suction cup's central axis, which could be useful in unpredictable objects and contexts.

3) *Tactile Images and Control:*

Regarding the informational value of the tactile images during all tests, assessing their difference images showcased meaningful tactile output data. Active pixels in the difference images emerged for differing the normal force, shear force, object shape, and the location of the object's center of gravity during lift. This highlights the potential of utilizing this tactile information for control and manipulation purposes in the future development of this design.

4) *Prediction Performance:*

The results of the orientation recognition experiment demonstrated that the Convolutional Neural Network successfully predicts latitude with an average absolute error of 1.97° and longitude with an average error of 9.41° . The suction cup is still able to close the seal with these error orders, as the passive compliance of the module proved to be effective in compensating for these predicted errors. Figure 13B indicates that the prediction errors for longitude display higher variance for a latitude value of zero degrees compared to other values. The cause for this would be that a latitude of zero automatically eliminates the longitude value, as no rotation takes place at all. As latitude increases, more markers undergo displacement, resulting in a higher signal-to-noise ratio and less variation, leading to shorter error bars.

Interestingly, the network's prediction performance did not show a discernible trend based on different indentations (Figure 14). Higher indentations were initially expected to yield a better performance due to increased marker displacement and improved signal-to-noise ratio. The explanation for this might be that the presence of higher indentation introduces more slip between the substrate and the suction cup, contributing to increased variation in the tactile images, which may cancel out the effect of having a stronger signal.

Analyzing the latitude error plot (Figure 13A), a slight decreasing trend is observed as the latitude value increases, passing through zero error at around 12° . This may be attributed to the fact that this experiment involved indirect deformations of the marker membranes, which occur through the transfer of deformation from the sucker infundibulum. This indirect mechanical filtering effect could result in lower prediction errors for certain 'preferred' latitude values, where the chosen architecture exhibits better transfer behavior.

Finally, to address potential variations in external light conditions and friction coefficients, future experiments could be extended over a longer period to capture different scenarios and enhance the network's ability to generalize under varied conditions. Additionally, the application of lubricant on the substrate could help reduce friction variations, although it may limit the network's performance if a different substrate material is used.

5) *Demonstration:*

During the demonstration (Appendix VI), it was discovered that using another, identical prototype drastically decreased the prediction performance when using it to correct the orientation in real life. Although the two printed versions of the prototype may have been identical in theory, manufacturing errors and manual post-processing steps such as the Plasti-Dip spraying process could induce slight variations. Therefore, the Convolutional Neural Network had to be trained again with training data from the new prototype before being able to successfully use it for live correction of the orientation. This finding suggests that it is highly recommended to train the network on multiple prototypes to make sure it can generalize on these variations. It is expected that this results in sufficient prediction performance on an previously unseen prototype as well.

Training the network with the second prototype resulted in similar error values compared to the original one. However, the prediction errors became larger when using the network on real angled objects. This may be caused by the fact that the used objects were made of a different material (aluminum) than the substrate it was trained on (plexiglass), which could cause frictional variations. Another reason could be that the visco-elastic nature of Agilus30Clear stretches the suction cup material over time, which could cause a different tactile image for the same orientation and indentation values.

B. *Future Work*

This work has primarily focused on training a Convolutional Neural Network to learn the relationship between tactile images taken and the orientation of the suction cup relative to a substrate. However, the tactile images acquired during the pull-off and pickup tests have also demonstrated the potential for sensing variations in normal force, shear force, object shape, and center of gravity. Future research could expand the machine learning framework and encompass this broader range of variables.

Another promising idea is to utilize the amount of membrane inflation before touching or exploring a surface as a sensitivity metric. By adjusting the degree of inflation, the suction cup's sensitivity to variations in surface stiffness can be fine-tuned. Actuating the fluidic circuit with a higher pressure reduces sensitivity to stiffness variations since there is less deformation sensed, thereby enabling the regulation of the signal-to-noise ratio accordingly. A possibility closely related to this is to analyze marker vibration patterns when sliding the suction cup over rough surfaces. These patterns could be used for haptic surface exploration and estimation of roughnesses. Studies by Huh et al. [3] and Wiertlewski et al.[13] provide valuable insights in this direction.

C. Challenges

While the high-resolution sensing capabilities of the proposed design are promising, the soft nature of the system remains a challenge. Unlike the octopus sucker, which can actuate and deform in three dimensions due to its muscular hydrostat structure [14], this work's suction cup is only driven by a single fluidic input. In contrast, the design's soft nature introduces numerous degrees of freedom. This discrepancy between high-resolution sensing and one-dimensional actuation poses a control challenge.

Lastly, this work has primarily focused on the development and evaluation of a single suction cup. However, integration of information from multiple suction cups to create a

comprehensive virtual environment representation still poses a challenge. As the number of suction cups increases, challenges arise in terms of data fusion, synchronization, and coordination. This task seems even more complex when considering that these limitations are, to some degree, even present in the octopus itself. For example, Wells' behavioral research [15], [16], [17] revealed that octopuses perceive object diameters based solely on the local curvatures of their suckers. As a result, a large diameter cylinder that is constructed of multiple smaller cylinders is actually perceived as its smaller counterpart. This finding highlights the difficulties that are involved in integrating the sensory information from multiple suction cups.

VII. CONCLUSION

Drawing inspiration from the architecture and sensing abilities of octopus suckers, a suction cup with high-resolution tactile sensing capabilities was developed. The sensing ability was realized by embedding colored markers acetabular roof and wall with the Chromatouch Principle. Tracking these markers with a camera produced tactile images containing useful information about forces, deformations and interactions with objects.

The results of the first experiment demonstrated the design's effectiveness for several practical applications. First, the suction cup exhibited a normal pull-off force of 9.35 N and a shear pull-off force of 5.28 N. It also showed the ability to successfully pick up a flat object, curved object, and a beam with a misaligned center of gravity. All of these experiments generated tactile images that contained useful information for control.

The results of the second experiment demonstrated the design's effectiveness in sensing the orientation with respect to a touching substrate. A Convolutional Neural Network was able to predict orientation only using a 100 x 100 pixel difference image taken during tilted contact. The achieved accuracy was an error of less than 2° for latitude (θ) and less than 10° for longitude (ϕ). This performance proved to be satisfactory for correcting the orientation and achieving perpendicular contact, essential to achieve a closed seal. This performance was validated by successfully using the network for recognizing and correcting the orientation and picking up four different angled objects.

In conclusion, the presented sensorized suction cup sets a starting point to overcome challenges in controlling soft robot arms. Integrating multiple of these modules in a soft arm and combining their sensed data could help to form a representation of the arm shape as a whole, which greatly simplifies control in unpredictable and turbid environments.

REFERENCES

- [1] Y. Tang, Y. Chi, J. Sun, T.-H. Huang, O. H. Maghsoudi, A. Spence, J. Zhao, H. Su, and J. Yin, "Leveraging elastic instabilities for amplified performance: Spine-inspired high-speed and high-force soft robots," *Science Advances*, vol. 6, no. 19, p. eaaz6912, 2020. [Online]. Available: <https://www.science.org/doi/abs/10.1126/sciadv.aaz6912>
- [2] C. Hegde, J. Su, J. M. R. Tan, K. He, X. Chen, and S. Magdassi, "Sensing in soft robotics," *ACS Nano*, vol. 17, no. 16, pp. 15 277–15 307, 2023, pMID: 37530475. [Online]. Available: <https://doi.org/10.1021/acsnano.3c04089>
- [3] T. M. Huh, K. Sanders, M. Danielczuk, M. Li, Y. Chen, K. Goldberg, and H. S. Stuart, "A multi-chamber smart suction cup for adaptive gripping and haptic exploration," in *2021 IEEE/RSJ International Conference on Intelligent Robots and Systems (IROS)*, 2021, Conference Proceedings, pp. 1786–1793.
- [4] S. Sareh, K. Althoefer, M. Li, Y. Noh, F. Tramacere, P. Sareh, E. J. Markvicka, and M. D. Bartlett, "Anchoring like octopus: Biologically inspired soft artificial sucker," *Journal of the Royal Society Interface*, vol. 14, no. 135, 2017.
- [5] S. T. Frey, A. Haque, R. Tutika, E. V. Krotz, C. Lee, C. B. Haverkamp, E. J. Markvicka, and M. D. Bartlett, "Octopus-inspired adhesive skins for intelligent and rapidly switchable underwater adhesion," *Sci Adv*, vol. 8, no. 28, p. eabq1905, 2022.
- [6] H. J. Lee, S. Baik, G. W. Hwang, J. H. Song, D. W. Kim, B. Y. Park, H. Min, J. K. Kim, J. S. Koh, T. H. Yang, and C. Pang, "An electronically perceptive bioinspired soft wet-adhesion actuator with carbon nanotube-based strain sensors," *ACS Nano*, vol. 15, no. 9, pp. 14 137–14 148, 2021.
- [7] E. Shahabi, F. Visentin, A. Mondini, and B. Mazzolai, "Octopus-inspired suction cups with embedded strain sensors for object recognition," *Advanced Intelligent Systems*, vol. 5, no. 2, p. 2200201, 2023. [Online]. Available: <https://onlinelibrary.wiley.com/doi/abs/10.1002/aisy.202200201>
- [8] X. Lin, L. Willemet, A. Bailleul, and M. Wiertelwski, "Curvature sensing with a spherical tactile sensor using the color-interference of a marker array," in *2020 IEEE International Conference on Robotics and Automation (ICRA)*, 2020, Conference Proceedings, pp. 603–609.
- [9] X. Lin and M. Wiertelwski, "Sensing the frictional state of a robotic skin via subtractive color mixing," *IEEE Robotics and Automation Letters*, vol. 4, no. 3, pp. 2386–2392, 2019.
- [10] R. B. N. Scharff, D. J. Boonstra, L. Willemet, X. Lin, and M. Wiertelwski, "Rapid manufacturing of color-based hemispherical soft tactile fingertips," in *2022 IEEE 5th International Conference on Soft Robotics (RoboSoft)*, 2022, Conference Proceedings, pp. 896–902.
- [11] D. Boonstra, "Learning to estimate the proximity of slip using high-resolution tactile sensing," master thesis, Delft University of Technology, 2022.
- [12] "Operations on arrays: Subtract()," OpenCV, 2023, [Accessed 15-08-2023]. [Online]. Available: https://docs.opencv.org/3.4/d2/de8/group_core_array.html#gaa0f00d98b4b5edeae7b8333b2de353b
- [13] M. Wiertelwski, J. Lozada, and V. Hayward, "The spatial spectrum of tangential skin displacement can encode tactual texture," *IEEE Transactions on*, vol. 27, pp. 461 – 472, 07 2011.
- [14] W. Kier and A. Smith, "The morphology and mechanics of octopus suckers," *Biological Bulletin*, vol. 178, no. 2, pp. 126–136, 1990.
- [15] M. Wells, "Tactile discrimination of surface curvature and shape by the octopus," *Journal of Experimental Biology*, vol. 41, no. 2, pp. 433–445, 1964.
- [16] —, "Taste by touch: Some experiments with octopus," *Journal of Experimental Biology*, vol. 40, no. 1, pp. 187–193, 1963.
- [17] M. Wells, N. H. Freeman, and M. Ashburner, "Some experiments on the chemotactile sense of octopuses," *Journal of Experimental Biology*, vol. 43, pp. 553–563, 1965.
- [18] F. Tramacere, N. M. Pugno, M. J. Kuba, and B. Mazzolai, "Unveiling the morphology of the acetabulum in octopus suckers and its role in attachment," *Interface Focus*, vol. 5, no. 1, p. 20140050, 2015.
- [19] M. Abadi, P. Barham, J. Chen, Z. Chen, A. Davis, J. Dean, M. Devin, S. Ghemawat, G. Irving, M. Isard *et al.*, "Tensorflow: A system for large-scale machine learning," in *12th {USENIX} Symposium on Operating Systems Design and Implementation ({OSDI} 16)*, 2016, pp. 265–283.
- [20] S. Wang, H. Luo, C. Linghu, and J. Song, "Elastic energy storage enabled magnetically actuated, octopus-inspired smart adhesive," *Advanced Functional Materials*, vol. 31, no. 9, p. 2009217, 2021. [Online]. Available: <https://doi.org/10.1002/adfm.202009217>
- [21] E. Shahabi, F. Visentin, A. Mondini, and B. Mazzolai, "Octopus-inspired suction cups with embedded strain sensors for object recognition," *Advanced Intelligent Systems*, vol. 5, no. 2, p. 2200201, 2023. [Online]. Available: <https://onlinelibrary.wiley.com/doi/abs/10.1002/aisy.202200201>
- [22] Y. Wang, G. Sun, Y. He, K. Zhou, and L. Zhu, "Octopus-inspired sucker to absorb soft tissues: stiffness gradient and acetabular protruberance improve the adsorption effect," *Bioinspir Biomim*, vol. 17, no. 3, 2022.

APPENDIX I

DESIGN PROCESS

A. Requirements

This part of the appendix explains the requirements that originate from the scenario in Figure 2 that was explained in the introduction (Section I). The requirements were formulated according to the three parts of the scenario. These were the exploration phase (Figure 2A), sealing and conforming phase (Figure 2B), and the tuning and manipulation phase (Figure 2C).

1) Exploration Phase:

During the exploration phase, the goal is to obtain a representation of objects and the environment, in order to plan an appropriate approach. The requirements belonging to this goal were formulated as follows. "Before attachment, the suction cup module should be able to ...

- ... Sense the **shape** and **position** of the substrate."
- ... Sense variations in **normal force**."
- ... Sense variations in **shear force**."

2) Sealing and Conforming Phase:

During the sealing and conforming phase, the goal is to adhere to a broad range of substrates. Therefore, this category of requirements consists of the following two. "The suction cup module should be able to ...

- ... Conform to **curved** surfaces."
- ... Conform to **rough** surfaces."

3) Tuning and Manipulation Phase:

During the tuning and manipulation phase, the goal is to use the sensed data for a balanced grip and adaptive manipulation. This category of requirements is formulated as follows. "During periods of attachment, the suction cup module should be able to ...

- ... Achieve a high **attachment force**."
- ... Withstand **collapse** due to low pressures."
- ... Sense the **shape** and **position** of the substrate."
- ... Sense variations in **normal force**."
- ... Sense variations in **shear force**."

B. Morphological Map

The requirements led to the creation of a morphological map. To come up with a broad range of ideas, three categories for brainstorming were defined for each requirement. These were the 'marker patterns and locations', the 'material properties' and the 'shape and morphology'. The result is shown in Figure A1. Then, three color codes were used to make combinations for creation of three different concepts. The concepts will be explained in the next section.

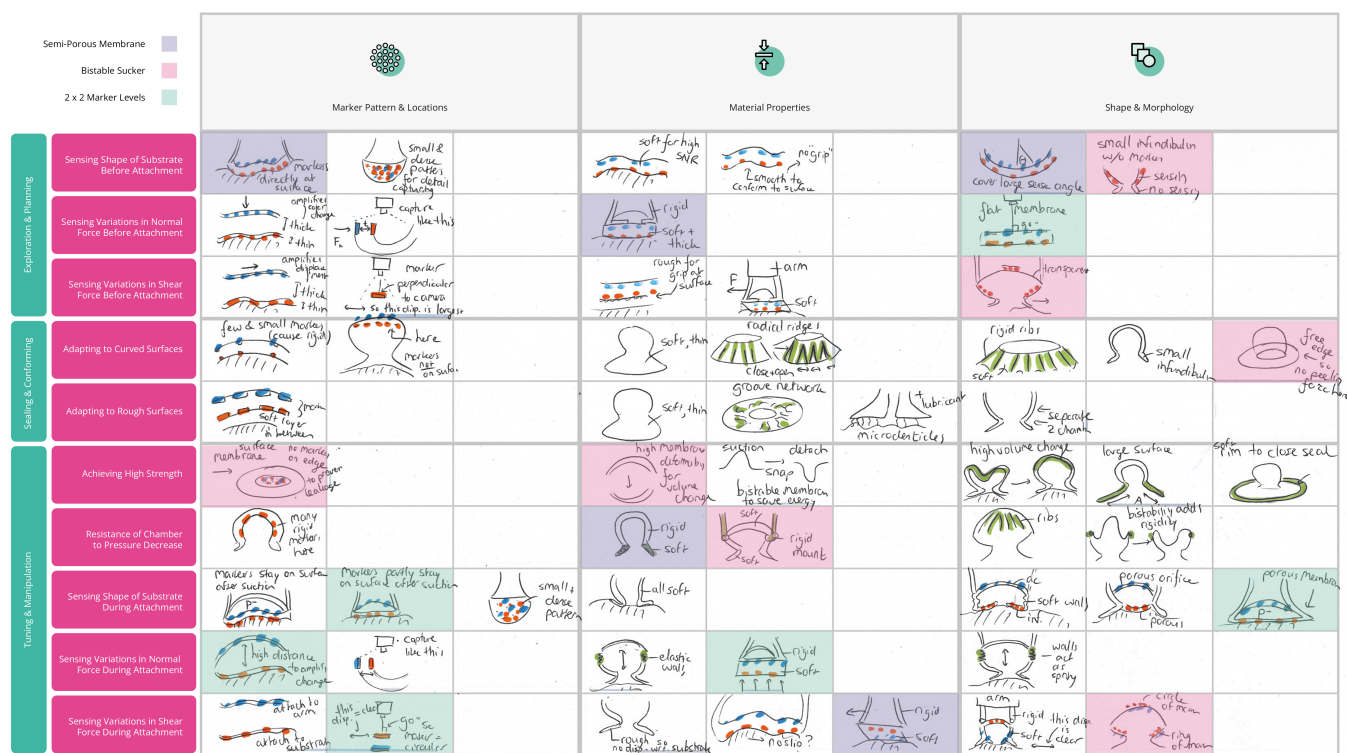


Fig. A1: Morphological map to create design solutions in three categories: 'marker pattern and locations', 'material properties' and 'shape and morphology'. Color codes are used to show the combinations that led to the development of three concepts

C. Concept Development

1) Concept 1: The Semi-Porous Membrane:

Figure A2 showcases the three developed concepts. The first concept (Figure A2A), the 'Semi-Porous Membrane', utilizes a two-layered membrane. During the exploration phase, the membrane obtains direct contact with the substrate, which leads to direct sensing of its shape and position. The outer layer is porous and will therefore stay attached to the substrate at all times. Activation of the vacuum pressure moves the inner layer upwards, while keeping the outer membrane attached to the substrate due to its porous nature. This way, marker deformations arising from interactions between the suction cup and the substrate will be visible at all times. Meanwhile, the inner layer of markers provides information about the pressure difference between the inner and outer layer. Figure A2A2 also shows the material distributions. A gradient stiffness design is used to make sure the bottom of the suction cup is soft and conformable, while the top gradually becomes stiffer to prevent collapse after the drop in pressure. This sub-figure also shows that Plasti-Dip is only applied on the outer layer. This way, the transparency of the inner layer is preserved and the outer markers will be visible through it.

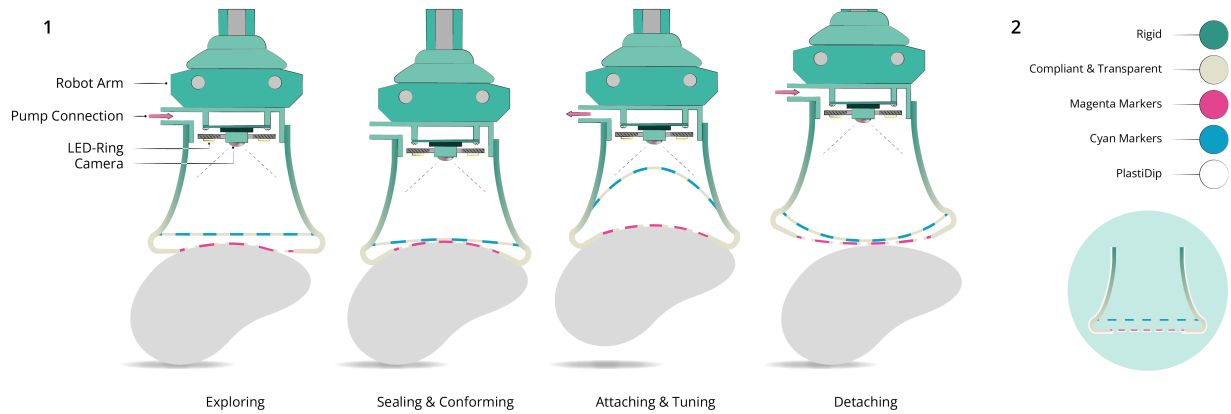
2) Concept 2: The Inverting Sucker:

The second concept (Figure A2B), the 'Inverting Sucker', is similar to the standard concept of a membrane-based fluidic suction cup, but makes use of a hinge-like structure to invert the membrane before and after attachment. Activation of the positive pressure puts the membrane in an inflated 'sensing' state. The bulging membrane enables the sucker to sense substrate shapes in a broad range of orientations. Activation of the vacuum retracts the membrane upwards and produces an attachment force. However, this makes the marker membrane completely lose contact with the substrate. Only indirect interactions between sucker and substrate caused by variations in volume of the chamber between them will now be visible. This design also adopts a stiffness gradient design (Figure A2B2). The soft parts encompass the conformable membrane and the elastic hinge structure that is able to easily switch between the states. The rigid part consists of the suction chamber that is thereby able to withstand collapsing after the pressure drop.

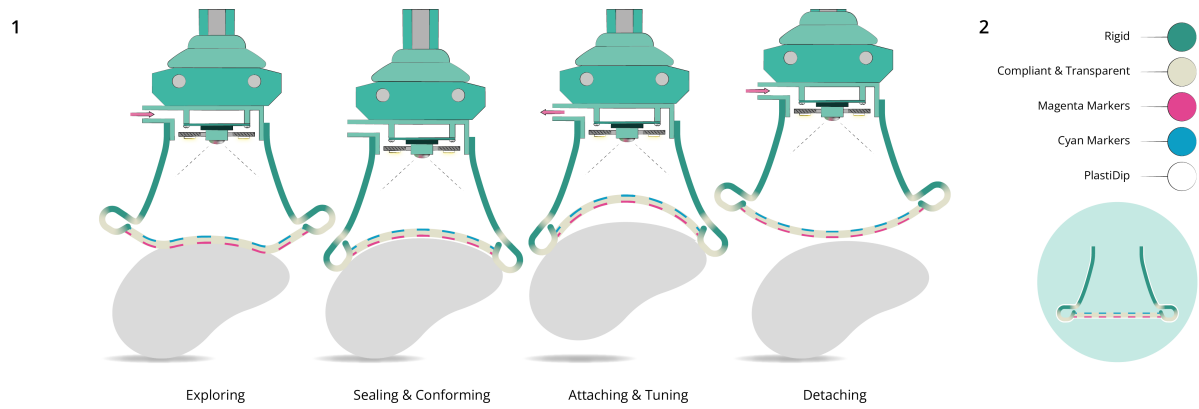
3) Concept 3: Double Marker Levels:

The third concept (Figure A2C), using 'Double Marker Levels', makes use of an octopus-inspired architecture with a clear division between the acetabular and infundibular portions. The acetabulum contains double layers of markers. The first (double) layer is located in the acetabular roof and is able to sense pressure variations by marker deformation caused by inflation and deflation. The second (double) layer is located in the acetabular wall and is able to sense more direct interactions between the substrate and suction cup. Figure A2C2 explains that this second layer of markers is visible through the transparent edges of the acetabular roof. Figure A22 reveals that no stiffness gradient is adopted for this concept. Instead, it is assumed that the rigid edge suffices to overcome the pressure drop and withstand collapse. Although this design never obtains direct contact with the substrate, unlike the other two concepts, it is expected that its architecture will still provide a rich amount of indirect information about force and contact interactions.

A. Semi-Porous Membrane



B. Inverting Sucker



C. Double Marker Levels

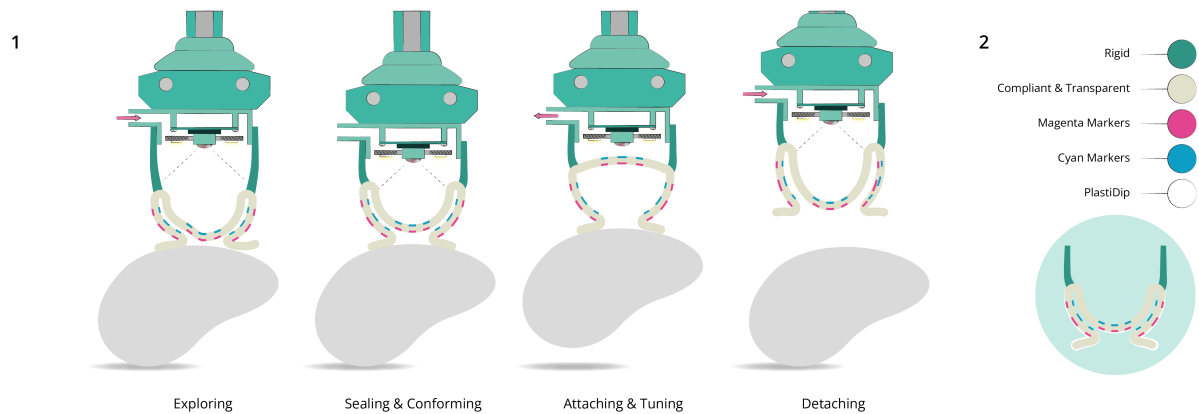


Fig. A2: Three design concepts. Sub-figure (1) of each concept shows the stages of the sensing and adhesion process, while sub-figure (2) shows the material distributions. (A) The Semi-Porous Membrane, using a closed upper membrane for obtaining the vacuum and a porous membrane to maintain contact with the substrate at all times. (B) The Inverting sucker, which uses a hinge-structure to easily switch between an inflated 'sensing' state and a deflated 'attached' state. (C) 'Double Marker Levels', which uses an octopus-inspired architecture that encompasses markers in both the acetabular roof and wall.

D. Concept Choice

Figure A3A lists the requirements obtained in Appendix Section I-A to use as a guideline for the concept assessment. In addition to this, two other categories of criteria have been added. The first is related to producibility and consists of a single criterion, 'the ease of support removal'. The second category relates to the expected quality of the design's tactile images, which is described by three criteria. First, the 'marker orientation with respect to the camera', which assumes that a more information-rich type of data is gathered when markers are oriented perpendicularly and appear as nearly circular. The second one is the 'marker clarity', which for example is influenced by the utilization of transparent membranes that decrease the visibility of the markers below it. The third criterion is the 'marker distance range'. It is expected that markers having a large difference in camera distance between adhesion states, are more difficult to get in focus at all times, and therefore decrease in visibility.

Figure A3B shows the assessment of each concept as a radar chart. It can be seen that the third concept, the octopus-inspired suction cup using double marker levels, obtains the highest score of 55 points. The most important considerations for this choice included the straightforward producibility compared to the other two concepts (ease of support removal and the lack of using a gradient stiffness design) and the fact that the octopus-inspired architecture would intuitively lead to a design that would function as intended.

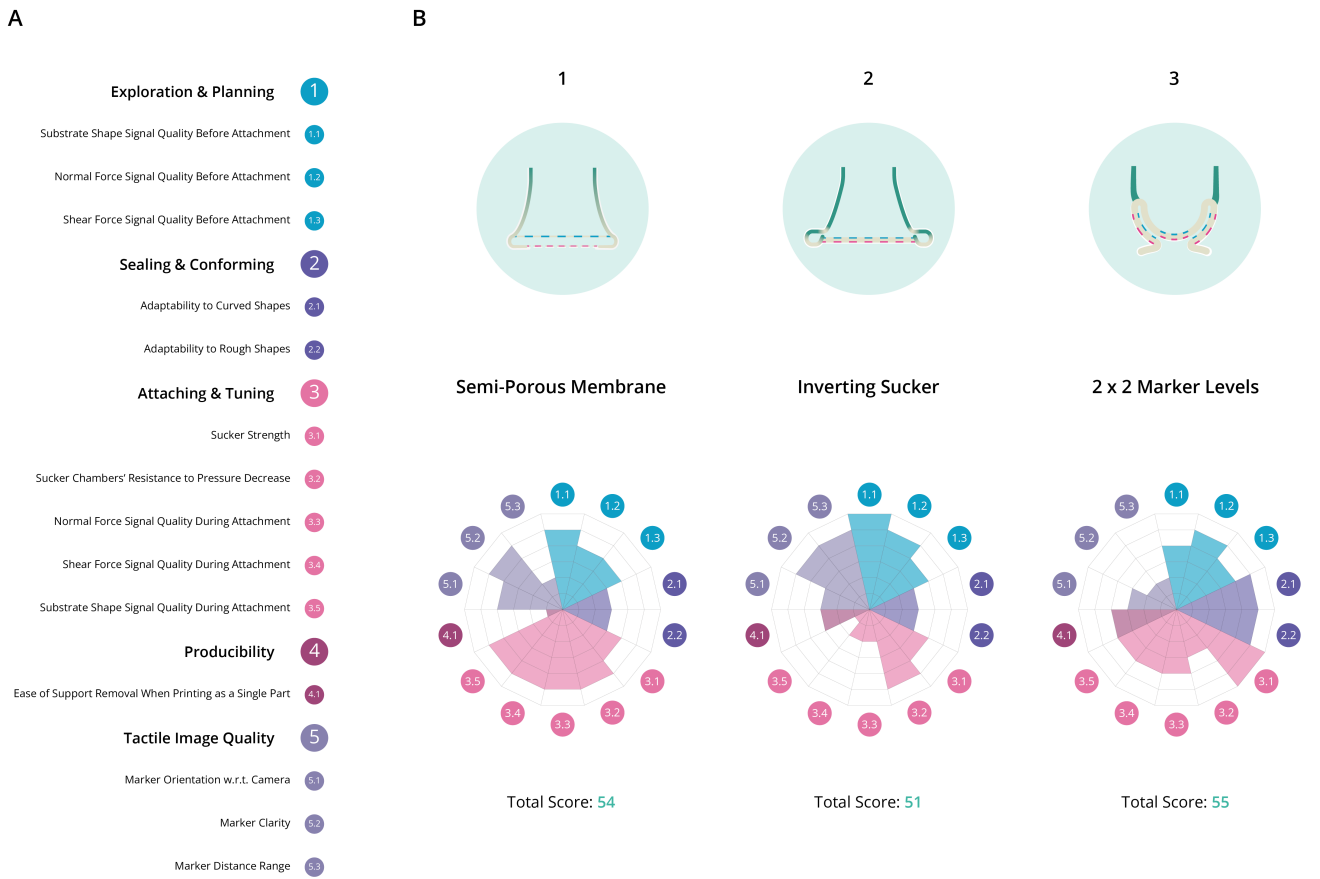


Fig. A3: **(A)** Listing of the criteria used for concept assessment, divided into five color-coded categories. **(B)** Radar charts that showcase the rating of each concept against the listed criteria.

A. Actuation Method

The literature study by van Veggel et al. (Appendix VIII-A) described that existing artificial suction cups employ various actuation methods, which encompass mechanical, fluidic, electric, thermal, and magnetic approaches. This work's design focuses on fluidic actuation, relying on an air pump and utilizing a membrane between the internal and external medium. A membrane-based fluidic actuation method offers several benefits:

- **Adjustability of attachment force:** Maximizing the benefits of a high-resolution sensing method also requires a high-resolution actuation method, rather than binary ON-OFF actuation. A membrane allows for adjusting the attachment force by modifying membrane retraction. This proves particularly advantageous when dealing with delicate or fragile objects.
- **Robustness to extreme environments:** The membrane facilitates use in wet and dry conditions because it functions as a shield against dust and contamination, protecting internal components and fluidic channels.
- **Light-blocking capabilities:** In combination with a diffuse outer layer, the membrane can block external light from interfering with the tactile images.
- **Prevention of leakage:** The membrane minimizes or eliminates fluidic leakage when the seal is not closed. This is especially useful in the case of employing multiple suction cups on a robot arm, actuated by the same fluidic circuit.

Figure A4A shows this commonly used architecture, consisting of a sucker body and a membrane. The working mechanism is shown in Figure A4B. After contact with a substrate is obtained (Figure A4B1 & B2), a pump facilitates retraction of the membrane (Figure A4B3). This causes a volume increase of the sealed chamber between the suction cup and the substrate, which results in a pressure drop that produces an attachment force (Figure A4B4).

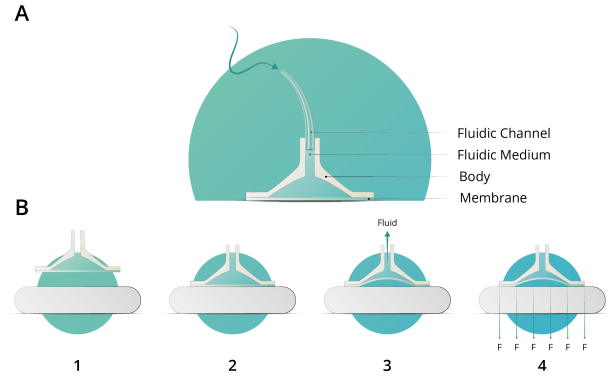


Fig. A4: Working principle of a fluidically actuated membrane-based suction cup. (A) Architecture and components and (B) Steps in the adhesion process. (B1) Approaching a substrate, (B2) Obtaining contact (B3) Retraction of the membrane leads to a volume increase of the chamber between the suction cup and the substrate, (B4) the resulting pressure drop produces an attachment force.

B. Octopus Inspiration

In Figure A5A, a simplified view of the octopus sucker is shown. Their suckers consist of two chambers, the infundibular chamber or 'infundibulum' and the acetabular chamber or 'acetabulum'. The infundibulum, characterized by its soft and compliant nature, conforms to the substrate shape and closes the seal. The acetabulum, which possesses a stiffer structure, generates the pressure drop through volume increase by contraction of radial muscles. These two chambers are connected through an orifice. Likewise, this work's design adopted a two-chamber approach. It aimed to mimic the conforming and sealing abilities of the octopus infundibulum while using the acetabulum to obtain the volume change required for the pressure drop and attachment force. The design is showcased in Figure A5B. The figure highlights the architectural similarities between the biological and the artificial suction cup. In Figure A6, the adhesion processes of both suckers are showcased. This clearly shows that the fluidic membrane actuation utilized in the artificial suction cup (Figure A6B) is used to replicate the function of the radial muscles in the octopus acetabulum (Figure A6A).

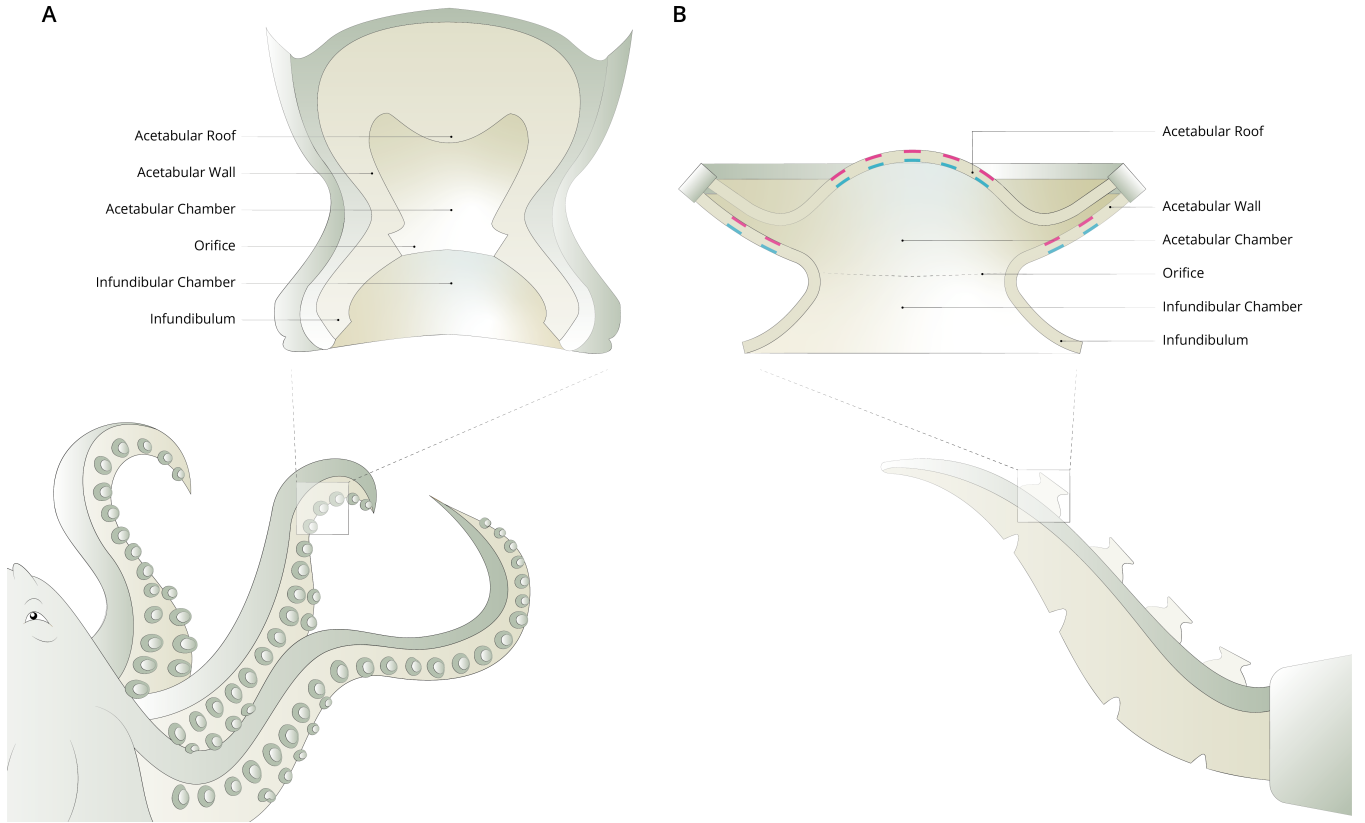


Fig. A5: Architectural similarities between (A) the Octopus *Vulgaris* Sucker and (B) the suction cup presented in this work.

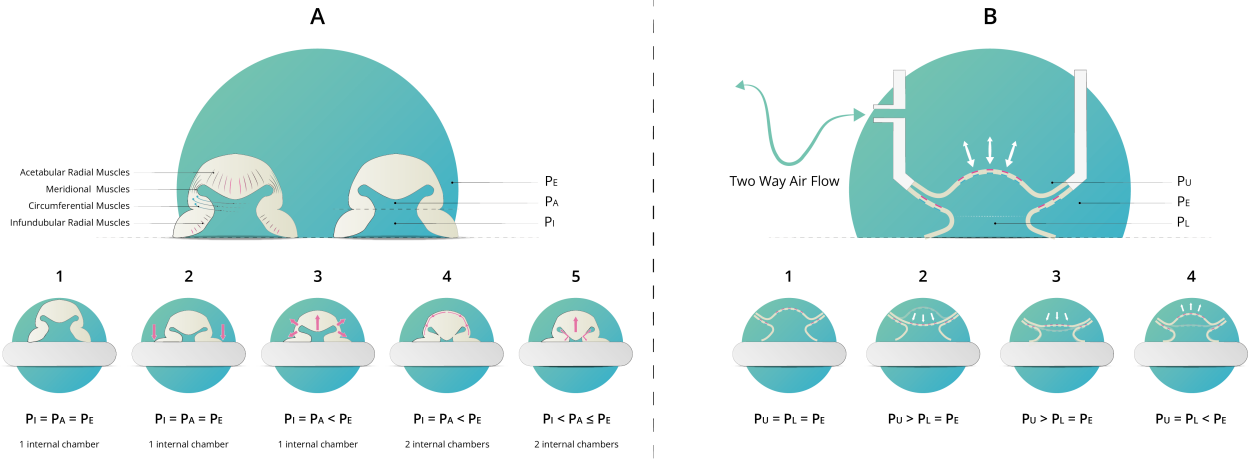


Fig. A6: Adhesion processes of both suction cups. (A) Adhesion process of the octopus sucker. (A1) Initial contact with the substrate, (A2) formation of a seal after contracting the infundibular radial muscles, (A3) pressure reduction through contraction of the acetabular radial muscles, (A4) interlocking of the protuberance in the orifice through contraction of the meridional muscles, and (A5) Continued adhesion after relaxing of the radial muscles due to the friction from hairs and ridges, cohesive forces of water and stored elastic energy in cross connective tissue fibres. Adapted from Tramacere et al. [18]. (B) Adhesion process of the the artificial sucker. (B1) Approaching the substrate with the membrane in a neutral state. All pressures are equal to atmospheric pressure P_E . (B2) Activation of the pump inflates the acetabular roof, increasing P_U . P_L is still equal to P_E as no seal has yet been achieved. (B3) Pressing the suction cup against the substrate forms a seal. (B4) Activation of the vacuum decreases P_U and thereby retracts the acetabular roof, increasing the volume of the chamber between the suction cup and the substrate. As this chamber is now sealed, this creates a pressure drop in P_L .

C. Marker Layer Samples

Using a second marker layer visible through a transparent membrane has not been employed in the previous versions of the Chromatouch sensor. To validate this possibility, a sample test with two dome-shaped membranes was conducted to compare four marker layout variations (Figure A7A1 – A4). Then, the threshold distance where the lower markers were still visible through the top membrane was determined (Figure A7B). Although variations in visibility existed between the alternatives, all of them exhibited sufficient performance at a threshold distance of 3 mm. Finally, the layout in Figure A7A3 was chosen because it was expected to provide the most information about the lower membrane. This layout incorporates both the magenta- and cyan color-filter in the lower marker layer.

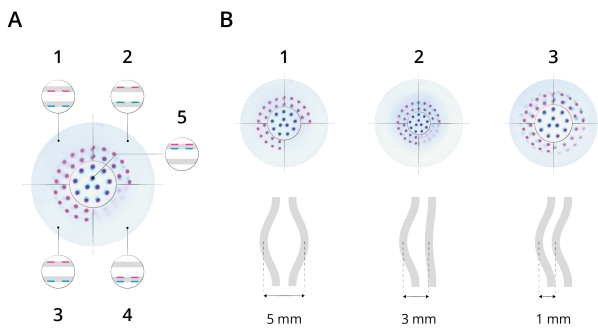


Fig. A7: (A) Four alternatives for marker placement in the lower membrane. (B) Determination of the threshold distance where the bottom marker layers are still visible through the transparent top membrane

D. Expected Example Signals

The two-layer marker architecture is expected to provide an information-rich type of image data. Examples are shown in Figure A8 and further explained below.

- The marker deformation in the acetabular roof offers information about the pressure difference between the chamber above and below it (P_U and P_L in Figure 5). This provides information about the fluidic actuation state (Figure A8A).
- The markers in the acetabular wall provide information about interactions with the external environment. Examples are the orientation with respect to an object (Figure A8B or sensing the object shape (Figure A8C).
- In case a seal is not formed (Figure A8D1), application of the vacuum results in a higher absolute pressure difference between the chamber above and below the acetabular roof, resulting in a more extreme deformation of the acetabular roof compared to when a seal is formed (Figure A8D2). This could potentially sense leakages.

- During pickup situations, the force interactions between the suction cup and the object will change the chamber shape. Due to air being trapped in this chamber, both the acetabular roof and wall will be affected by this. Their deformation patterns may provide information about the direction and magnitude of these forces. (Figure A8E).

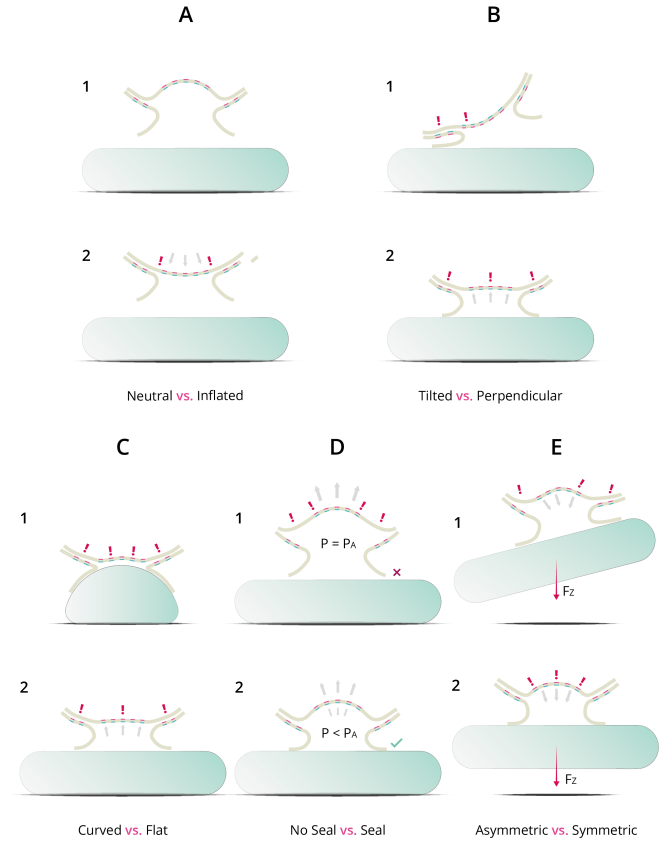


Fig. A8: Theoretical scenarios causing membrane deformation, expected to produce information-rich image data. (A) Fluidic actuation in (A1) Neutral (off-) state vs. (A2) an inflated acetabular roof. (B) Indentation with (B1) Tilted contact, where the infundibular surface acts as a mechanical lever to transfer information to the acetabular wall and roof vs. (B2) Perpendicular contact with a sealed chamber. The chamber is sealed and the trapped air is subject to volume conservation, so the change of the chamber shape due to indentation results in an upwards deformation of the acetabular roof. (C) Sensing objects with (C1) a curved shape vs. (C2) a flat shape, showing a different deformation of the acetabular roof and wall. (D) Application of vacuum pressure (D1) without a seal vs. (D2) with a seal, showing a clear difference in deformation of the acetabular roof. (E) Picking up an object with (E1) the center of gravity misaligned with the suction cup, showing asymmetrical deformations of the acetabular roof and wall, vs. (E2) the center of gravity aligned with the suction cup, showing symmetrical deformations of the acetabular roof and wall

E. Parametric Modelling

The suction cup was parametrically modelled in Rhino Grasshopper. This aided rapid comparison of variations, and experimenting with different geometrical parameter values. Although the Grasshopper model contained 32 variable parameters, the ones selected here are those assumed to be most influential on the theoretical attachment force and sensing resolution. The force-related parameters are the ones affecting the volume change before and after adhesion. These include the infundibulum angle (θ_i), acetabulum angle (θ_a), infundibulum radius (r_i), and acetabulum height (h_a). The sensing-related parameters are the ones influencing the marker density. These include the number of markers on the upper and lower membrane (N_U and N_L), along with the marker diameter (d_m). The parameters are illustrated in Figure A9B. To simplify the analysis, the number of markers on the upper membrane was set to half of the number on the lower membrane for every configuration, reducing the number of parameters from seven to six. The table in Figure A9A presents three variants for each parameter, theoretically resulting in $3^6 = 729$ possible combinations. However, as assessing and displaying each combination would be too time-consuming, six random variants were displayed to explore different possibilities and assess the influence of their variation. The header row of the table displays the top, isometric, and front views of each configuration, respectively. Since we were only interested in the effect of relative variations between parameter values, the global scale of the suction cup remained unchanged in each configuration. This was achieved by setting the edge radius to 30 mm and the orifice radius to 8 mm. The membrane and marker thicknesses were replicated from the most recent Chromatouch sensor in Scharff et al. [10].

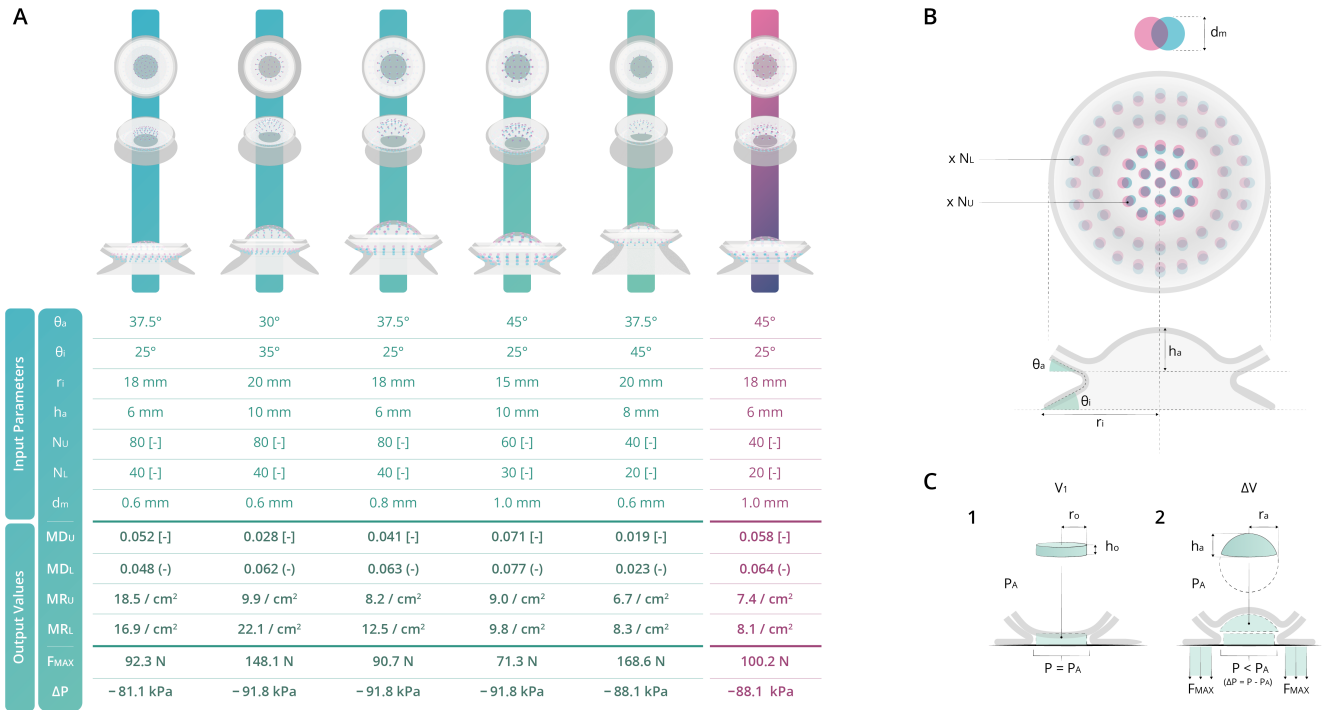


Fig. A9: **(A)** varying seven geometrical parameters in Rhino Grasshopper to obtain six configurations of the suction cup. The bottom of the table displays the influence of the parameters on output variables related to sensing (M_D = Marker Density as the surface ratio of total marker area to membrane area, M_R = Marker Resolution in markers/cm²). The outer right configuration was finally selected to continue with **(B)** Visualization where the parameters are located. **(C)** The simplified geometrical models used for the theoretical force and pressure calculations. **(C1)** Volume of internal chamber before application of the vacuum and **(C2)** after application of the vacuum.

1) Effect of Parameter Variation:

To demonstrate the influence of parameter variation, the six bottom rows of the table in Figure A9A show six output values for each configuration. These include the marker density in the acetabular roof (MD_U) and wall (MD_L), which are expressed as the surface ratio between marker area and the total membrane area. On the one hand, displacement of larger markers is easier to track in the images and leads to an improved signal-to-noise ratio (SNR). However, as the Polyjet materials available for the markers are only available as rigid resins, a higher marker density would result in worse deformation properties of the suction cup.

The output values below these are the marker resolution in the acetabular roof (MR_U) and wall (MR_L), which signify the number of markers per cm^2 . As discussed in Scharff et al. [10], the Nyquist Theorem states that membrane deformations down to the size of two markers could theoretically be observed. The final two values are the theoretical pressure change (ΔP) and maximum attachment force (F_{MAX}). Calculation of these values employs the ideal gas law, assuming a conservation of $P \cdot V$ under a constant gas temperature. The initial volume V_1 (Figure A9C1) represents the inflated state of the acetabular roof with the pressure equal to atmospheric pressure P_A . Considering the infundibular surface fully flat on the substrate before activating the vacuum pressure. The volume representing the orifice, V_1 , is approximated as a circular disk with height h_o and radius r_o , giving $V_1 = \pi \cdot r_o^2 \cdot h_o$. Activation of the vacuum retracts the acetabular roof upwards, increasing the chamber volume between the substrate and the suction cup by ΔV , which is approximated as a spherical cap with height h_a and sphere radius r_a . The volume of this cap is calculated as $\frac{1}{3} \pi \cdot h_a^2 (3 \cdot r_a - h_a)$. By using the ideal gas law equation $P_A \cdot V_1 = P \cdot (V_1 + \Delta V)$, we calculate P as $P_A \cdot \left(\frac{V_1}{V_1 + \Delta V} \right)$. The pressure change is then expressed as $\Delta P = P - P_A$. To calculate the force, the absolute pressure change is multiplied by the infundibular surface area, considering it flat with a surface area of $A_i = \pi \cdot \left(r_o + \frac{r_i - r_o}{\cos(\theta_i)} \right)^2$. Assuming even pressure distribution over the infundibular surface, the theoretical maximum attachment force then becomes

$$F_{\text{MAX}} = A_i \cdot |\Delta P|.$$

While the optimal parameter values have not been established yet, this research aims to demonstrate the proof of concept rather than identifying the best configuration. Educated guesses led to selecting the purple version in Figure A9A.

2) Marker Pattern:

The marker-embedded portions of the acetabular roof and wall were modelled as parts of a sphere surface. This enabled the use of the Deserno Algorithm, also used in the most recent version of the ChromaTouch sensor [10], to divide markers over the surface. The algorithm is visualized in Figure A10. It takes an arbitrary number of markers N , sphere midpoint location (x, y, z) , sphere radius R and angular domain $[\theta_L, \theta_U]$ as inputs. It then generates a collection of points on the surface, while ensuring the average marker area A_M remains the same and approaches a square ($d\theta \approx d\phi$). This ensures a uniform sampling resolution in the tactile images. The generated points form the centers of cones with their base normal to the sphere surface, and diameter equal to the chosen marker diameter. The intersection between these cones and the inner and outer membrane layers defines the marker volumes.

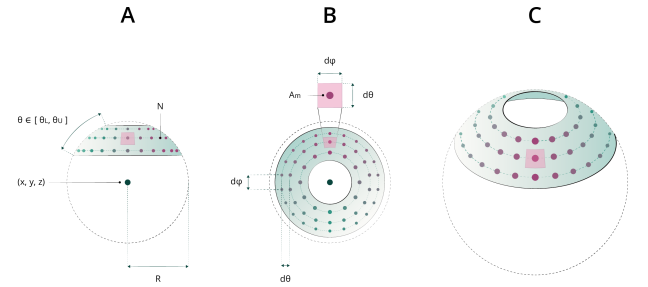


Fig. A10: Adapted Deserno Algorithm to generate a collection of points on a spherical surface, to form the basis for marker modelling. **(A)** Inputs of the algorithm: Number of markers N , sphere midpoint (x, y, z) , sphere radius R and angular domain $[\theta_L, \theta_U]$. **(B)** Ensuring that the area A_M surrounding each point is equal for all points and approximates a square so $d\theta \approx d\phi$. **(C)** 3D view of the point collection

APPENDIX III

PROTOTYPE VERSIONS

A. Prototype Version A

Figure A11 shows three different versions of the prototype. The first version (Figure A11A) is the one that was used for the experiments. This version is printed in a top part and a bottom part that were assembled with silicon glue afterwards.

B. Prototype Version B

The second version (Figure A11B) was printed in a single part. Although it turned out that this was possible, it made the removal of the support material significantly more complicated. This design also consisted of a rim with a circular cross-section around the infundibulum edge, of which it was expected that it would help closing the seal between the suction cup and the substrate. It also encompassed a rough structure, which we called 'microdenticles' on the infundibular surface. The expectation was that this structure would help divide the pressure over the entire infundibular surface by creating a network of air channels. Both of these additions to the architecture were inspired by the octopus sucker morphology as explained in the Literature Review of van Veggel et al. (Appendix VIII-A). However, as their combination with the Plasti-Dip layer quickly showcased formations of cracks and flaking, it was decided not to continue with this variant in the experiment.

C. Prototype Version C

The third version (Figure A11C) was a proof-of-concept test of the gradient stiffness that was earlier described in Appendix Section I-C. Only the bottom part of the suction cup, encompassing the acetabular wall and the infundibular surface, was used to test this. The Grasshopper VoxelPrinting plugin enabled to convert all parts of the design to voxels and assign a separate material to each individual voxel. This way, it was possible to create a stiffness gradient ranging from the infundibulum (soft and elastic) to the acetabulum (rigid). This was obtained by the plane gradient function. This function determines the material ratio between the soft (Agilus30Clear) and rigid (VeroClear) material of in each printed 'slice' by making it linearly dependent on its distance to a plane. This plane was located at the slotted edge. It resulted in a material ratio that started from 100 % rigid / 0 % soft at this edge and ranged to 0 % rigid / 100 % soft / at the orifice. The print showed that the stiffness gradient design certainly has potential for future versions. However, due to the computationally intensive nature of the voxelizing process, a downsampling of a factor 6 was necessary to apply the stiffness gradient. This resulted in a rather 'pixelized' print, that was unsuitable to continue experiments with.

A. Two Separate Parts

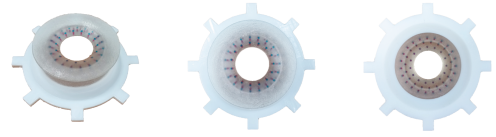
1. Top Before Plastidip



2. Top After Plastidip



1. Bottom Before Plastidip

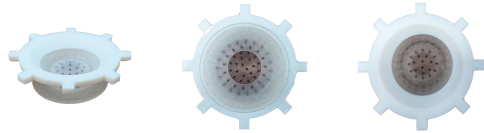


2. Bottom After Plastidip



B. Single Part, Rim, Denticles

1. Before Plastidip

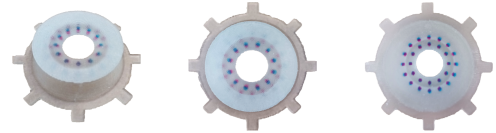


2. After Plastidip



C. Stiffness Gradient with VoxelPrinting

1. Before Plastidip



2. After Plastidip



Fig. A11: Three different versions of the design. Sub-figure (1) Shows the 'raw' print directly after support removal, while sub-figure (2) of each version shows the design after application of the Plasti-Dip layer. (A) Version A, with the top and bottom printed separately and the use of a simple architecture without a rim or denticles. (B) Version B, with the top and bottom printed in a single part, a rim around the infundibular edge and a rough 'denticle' structure on the surface of the infundibulum. (C) Version C, for which only the bottom part has been printed to test the use of a stiffness gradient obtained by voxelprinting. The stiffness gradient ranges from a rigid acetabulum to a soft and conformable infundibulum.

APPENDIX IV NETWORK ARCHITECTURE

A. Hyperparameter Grid Search

After applying a $3 \times 3 \times 3$ grid search for the hyperparameters ‘kernel window-size’, ‘learning rate’ and ‘initial number of kernels’ (halved in each next convolutional layer), the hyperparameter set with the smallest validation loss was chosen to continue with. This corresponded to a 5×5 kernel window, a learning rate of 0.001 and 20 kernels in the first convolutional layer. The results of the grid search process is shown in Figure A12.

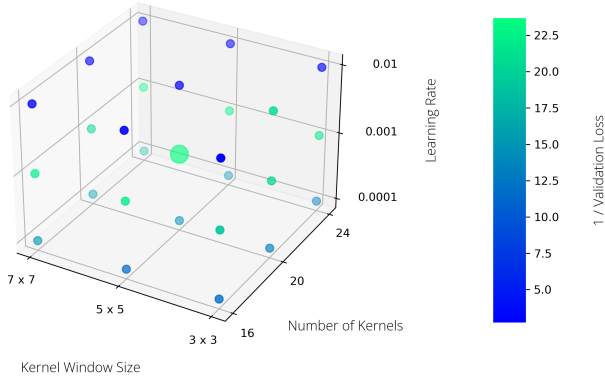


Fig. A12: Grid Search process for hyperparameters ‘kernel window-size’, ‘number of kernels’ and ‘learning rate’. For visualization purposes, the inverse of the validation loss $\frac{1}{\text{Val.Loss}}$ is plotted.

B. CNN Architecture

The architecture resulting from the grid search process is visualized in Figure A13. The input dimension of the network was set to $100 \times 100 \times 4$, corresponding to the RGBA values of the tactile images, normalized between zero and one. Then, three sequences of convolution, each with ReLu activation, and followed by a 2×2 Max Pooling layer were used. The output was flattened and fed into three output nodes. These three output nodes corresponded to the prediction of the latitude value, normalized between zero and one ($\hat{\theta}$), and the sine and cosine of the longitude value ($\sin(\phi)$ and $\cos(\phi)$). This deconstruction of the longitude value was used to eliminate large prediction errors close to an entire revolution. The images were randomly divided into training, validation and test data with percentages of 0.7, 0.15 and 0.15 respectively.

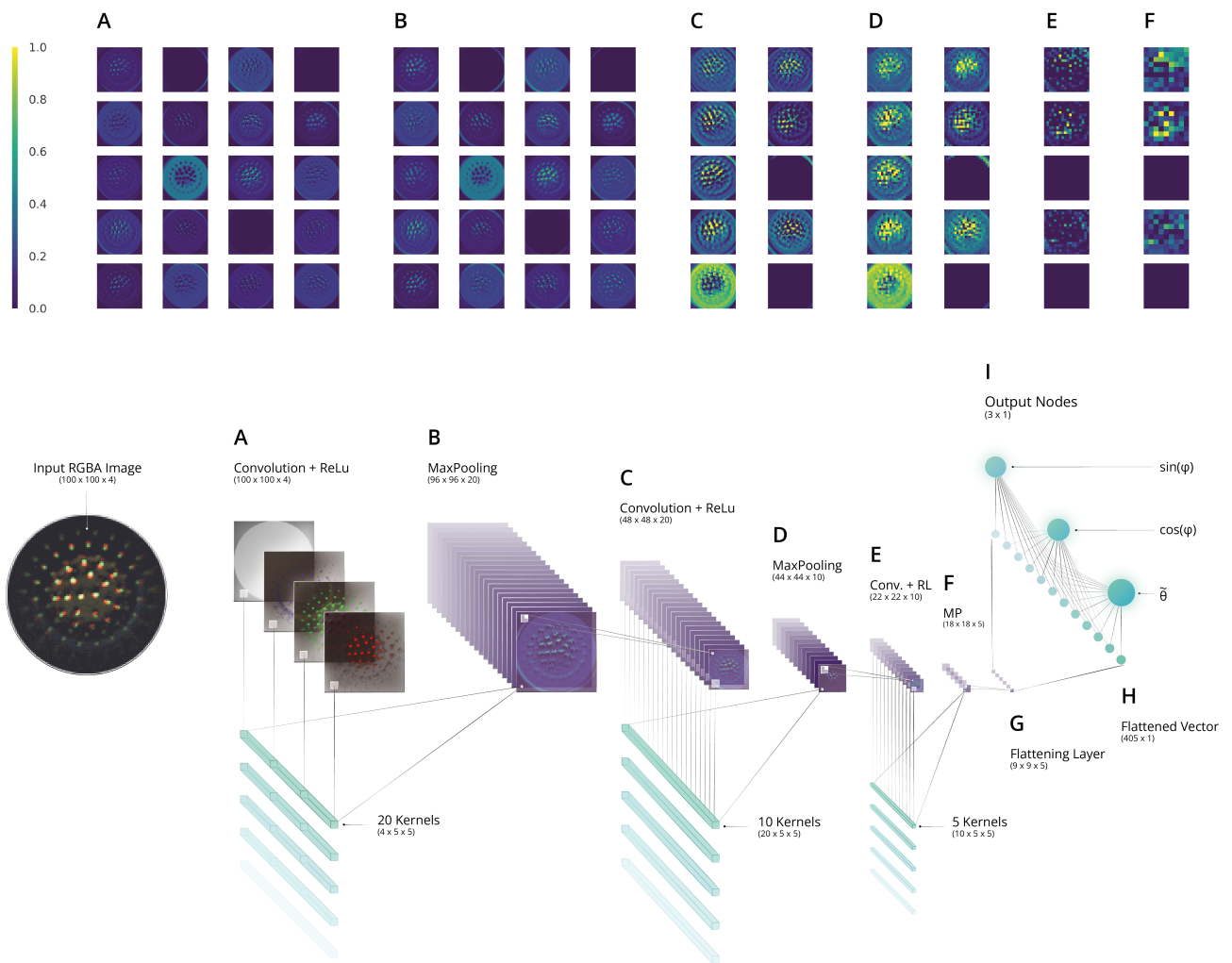


Fig. A13: Visualization of the CNN's Architecture. **(A)** The RGBA input image is fed into the first convolutional layer. **(B)** A Max Pooling operation is performed on the output of convolution. **(C-F)** The network feeds the image into two more sequences of convolution and pooling **(G-H)** The output of the final pooling layer is flattened. **(I)** The flattened vector is fed into three output nodes corresponding to the sine and the cosine of the longitude ($\sin(\phi)$ and $\cos(\phi)$) and the normalized latitude value (θ).

The kernel is used for feature extraction and feature mapping, which helps in learning relevant patterns. It can be thought of as a smaller template of a feature that can be present in the image, for example, an edge, blob or certain marker configuration. The kernel slides over the image and detects the amount of match or overlap of the feature at each location. The total amount of overlap in the kernel at that location is then used to obtain the new pixel value of the output image. A high amount of overlap with a certain kernel thereby corresponds to a high pixel value in the output image, it can be said that the network then fires on that feature. Training the network actually means that the network learns which features it should recognize to obtain the best match between the training images and the training labels.

Looking at this in more detail, the kernel is actually a three-dimensional matrix containing parameter values. Each parameter is multiplied with the normalized (between zero and one) pixel value at the current location in the input image. To obtain the new pixel value at that location in the output image, the multiplication results are summed and a bias is added. Training the network is a process of tuning the kernel's parameter values, which regulates how sensitive the network becomes to certain combinations of patterns of pixel values in the input image. The top part of Figure A13 shows the course of the pixel output values after each layer when feeding a random input image into the trained network.

The size of the kernel window is 5×5 pixels. Its depth corresponds to the number of channels in the input of the convolutional layer. For the input image, the amount of channels is 4 due to the RGBA format, which means that the kernel can be thought of as a 3D matrix of $5 \times 5 \times 4$ parameter values (see Figure A13A). As the sliding process is unable to continue when the kernel reaches the border of the image, the kernel can only slide 96 times in each dimension. Therefore, each output image of this convolutional layer will only be 96×96 pixels.

Because we have 20 kernels in this layer, the output of the first convolutional layer is a stack of 20 new 96×96 images with pixel values lying between zero and 1. This can be thought of as the image now containing 20 channels, similar to the input image having 4 channels. The dimensions of our image are now $96 \times 96 \times 20$ (see Figure A13B).

After the convolutional layer, a 2×2 Max Pooling layer is applied. This means that each set of 2×2 pixels in the images will be replaced by the highest value of those four, which reduces the dimension of the image to 48×48 pixels. The dimensions of the image are now decreased to $48 \times 48 \times 20$ (see Figure A13C).

The sequence of convolution followed by pooling is applied three times in total (Figure A13C-G). The amount of kernels is halved in each next convolutional layer, so comes down to 20, 10 and 5 kernels respectively. The kernel window size is 5×5 pixels each time. After all convolution and pooling operations, the dimensions are reduced to $9 \times 9 \times 5$ (see Figure A13G).

The pixel values of this final image are flattened into a single vector of dimension 405×1 (Figure A13H), which are then fed into three output nodes that correspond to the sine and the cosine of the longitude ($\sin(\phi)$ and $\cos(\phi)$) and the normalized latitude ($\tilde{\theta}$).

To investigate the number of total trainable parameters of this network:

- The first convolutional layer has a 5×5 kernel window which is used on an input of 4 channels. There are 20 of these kernels, which adds up to $5 \times 5 \times 4 \times 20 = 2000$ parameters. For each kernel, a bias is added at the end, which results in $2000 + 20 = 2020$ parameters for this layer in total.
- When applying the same calculation for the other two convolutional layers, this results in $5 \times 5 \times 20 \times 10 + 10 = 5010$ parameters for the second layer, and $5 \times 5 \times 10 \times 5 + 5 = 1255$ parameters for the third layer.
- The pooling and flattening layers do not involve any trainable parameters.
- Feeding the 405×1 flattened pixel values into the three output nodes involves $405 \times 3 = 1215$ trainable parameters. Here, a bias is added to each node as well, which adds three more parameters. This adds up to $1215 + 3 = 1218$ parameters for this operation.
- The total amount of trainable parameters then comes down to $2020 + 5010 + 1255 + 1215 = 9500$ parameters.

C. Training Results

This final version of the CNN was trained in approximately 7 minutes (14 s per epoch for 30 epochs). This resulted in a training MSE of 0.044 and a validation MSE of 0.042. The training and validation curves are shown in Figure A14. To get a more intuitive look on the CNN performance, Figure A15 shows the results of feeding four random difference images from the test set to the network.

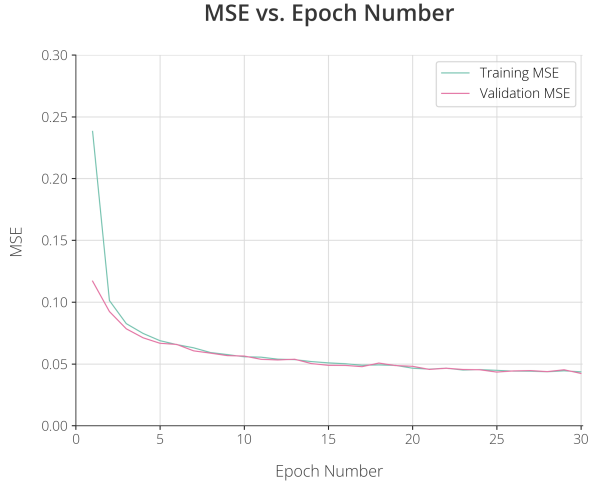


Fig. A14: Training and validation curve of the CNN, constructed of the optimal hyperparameter set determined in Appendix Section IV-A

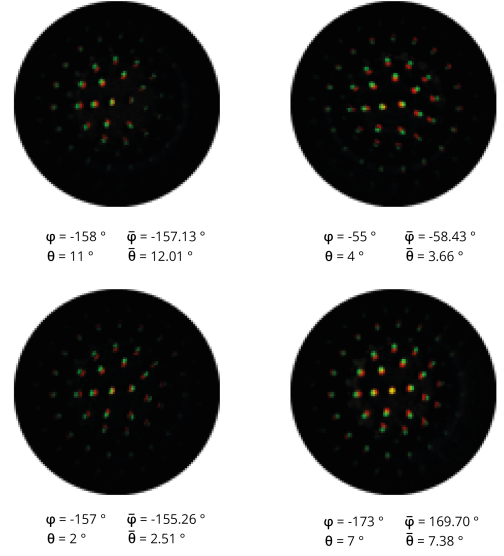


Fig. A15: Prediction results of the CNN after feeding it four random difference images from the test set.

APPENDIX V SUPPLEMENTARY RESULTS

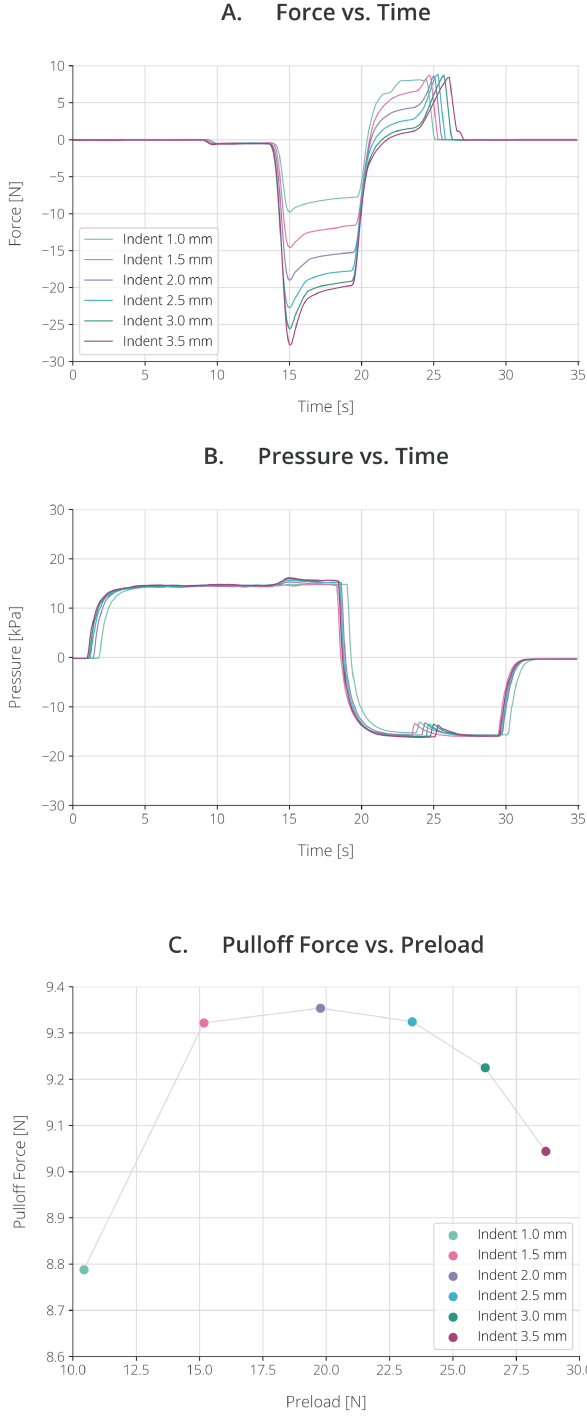


Fig. A16: **(A)** Force-, and **(B)** pressure plot for indentation levels ranging from 1.0 mm to 3.5 mm. **(C)** Normal pulloff force plotted against preload for each level of indentation.

A. Determination of Optimal Pulloff Force

The force and pressure- plots of the pull-off tests for every indentation are shown in Figure A16A and B. It became clear that an indentation of 2.0 mm produced the optimal pulloff force of 9.35 N, with a corresponding preload of 22.2 N (Figure A16C). This was achieved by activating the fluidic circuit with a positive input pressure of 15.28 kPa, followed by a negative pressure of -15.77 kPa.

B. Prediction Results for Separate Indentations

Figure A17 shows the prediction error for the latitude (θ , in Figure A17A) and longitude (ϕ , in Figure A17B), separated for each indentation. This plot provides insight into the CNN's generalization behavior over the indentation depth.

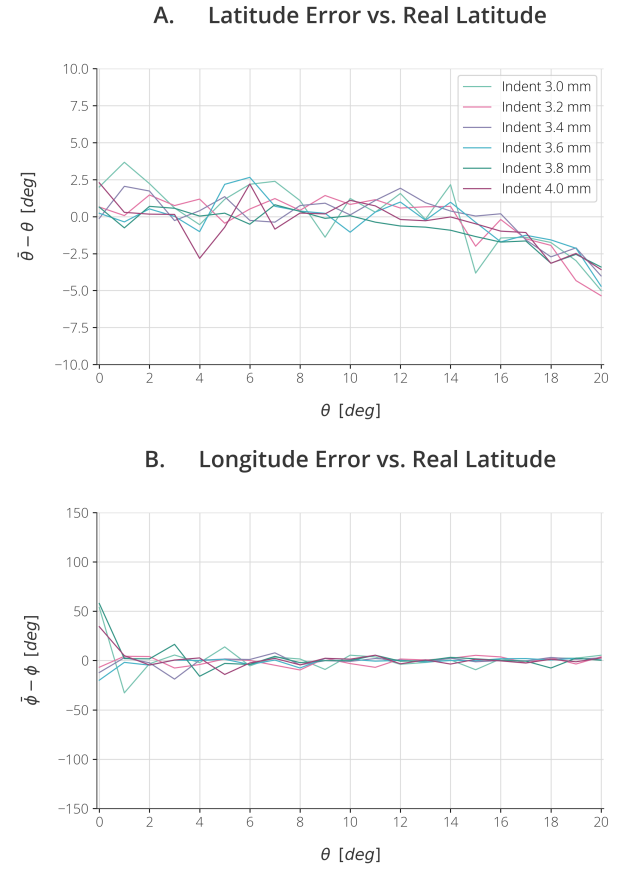


Fig. A17: **(A)** latitude (θ) and **(B)** longitude (ϕ) prediction errors, plotted against real latitude values and separated per indentation value

APPENDIX VI DEMONSTRATION

This Appendix evaluates if the theoretical performance of the Convolutional Neural Network would be satisfactory for real life pickup scenarios. First, it was investigated whether the suction cup's passive compliance would suffice to correct for the Convolutional Neural Network's prediction error values. For this, a pickup test without any correction was performed. The substrate was placed in an orientation with values comparable to the average prediction errors. Next, the ability to actively correct the orientation and obtain perpendicular seals was tested. For this, pickup tests in with objects in four different orientations were performed. In these tests, the Convolutional Neural Network was used to recognize the relative orientation and orient the suction cup correctly to pick up the objects.

A. Passive Correction

In order to see if the average prediction errors of the Convolutional Neural Network would suffice in real life pickup scenarios, a pickup test was performed with the relative orientation of the object representing the error orders. The average absolute latitude prediction error ($|\theta - \bar{\theta}|$) was 1.97° and the longitude prediction error ($|\phi - \bar{\phi}|$) was 9.41° . Therefore, the object was placed in an inclination (representing the latitude) of 2° and a rotation (representing the longitude) of 10° . The used object was the same as the one used in Figure 12A. The result of this pickup test is shown in Figure A18 and can be found as a video in Appendix IX-D. It is clearly visible that the suction cup shows a tilted deformation to conform the the object's orientation. Then, it forms a seal, activates the vacuum and successfully lifts the object. This result proves that the passive compliance of the suction cup suffices to correct for the prediction error orders, and still obtain a seal between the substrate and the suction cup.

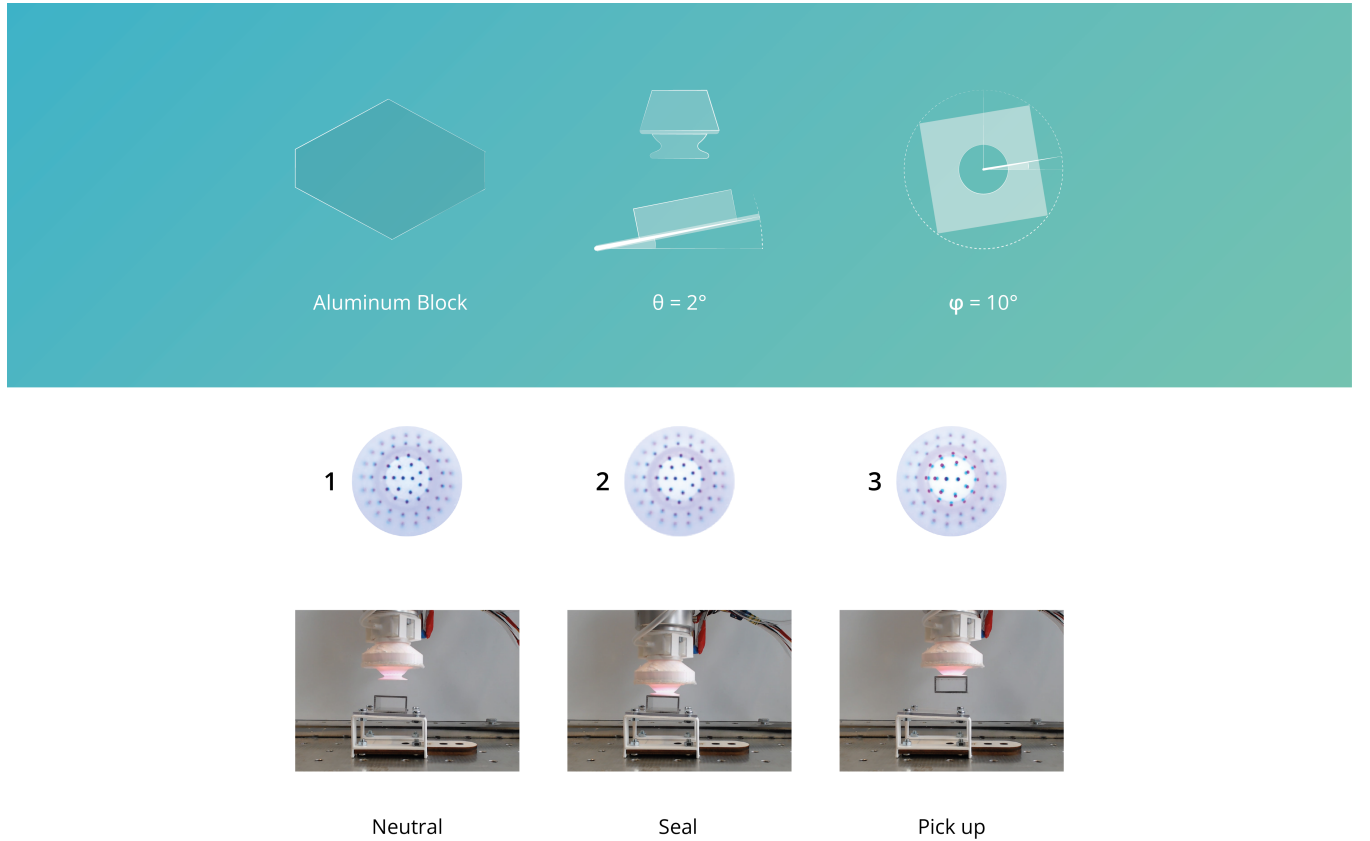


Fig. A18: Picking up an object oriented in latitude (θ) and longitude (ϕ) values comparable to the Convolutional Neural Network's prediction errors. This corresponded to a latitude (θ) value of 2° and a longitude (ϕ) value of 10° .

B. Active Correction

The original Convolutional Neural Network was coded in Tensorflow [19]. However, the Raspberry Pi was not suitable for the Tensorflow python library. Therefore, the network was first converted to a Tensorflow Lite (TFLite) version before importing it onto the device. Then, four pickup tests were performed and the network was used to orient the suction cup correctly, in order to successfully pick up the object. This is shown in Figure A19. Objects were placed into four different orientations. The latitude (θ) values started at 5° (Figure A19A) and was incremented with 5° each time (A19B-D). The longitude (ϕ) started at 0° (Figure A19A) and was incremented with 45° each time (Figure A19B-D). Difference images (before vs. after the tilted indentation) were obtained in the same way as used in the data collection process explained in Figure 9. The image was then fed to the neural network and the output values were used to calculate the relative orientation. This result was used to orient the suction cup perpendicularly above the object, and achieve a seal. Although it showed that the prediction errors in the pickup test were larger than the theoretical ones, It still resulted in all four objects being successfully picked up. Videos can be found in Appendix IX-E.

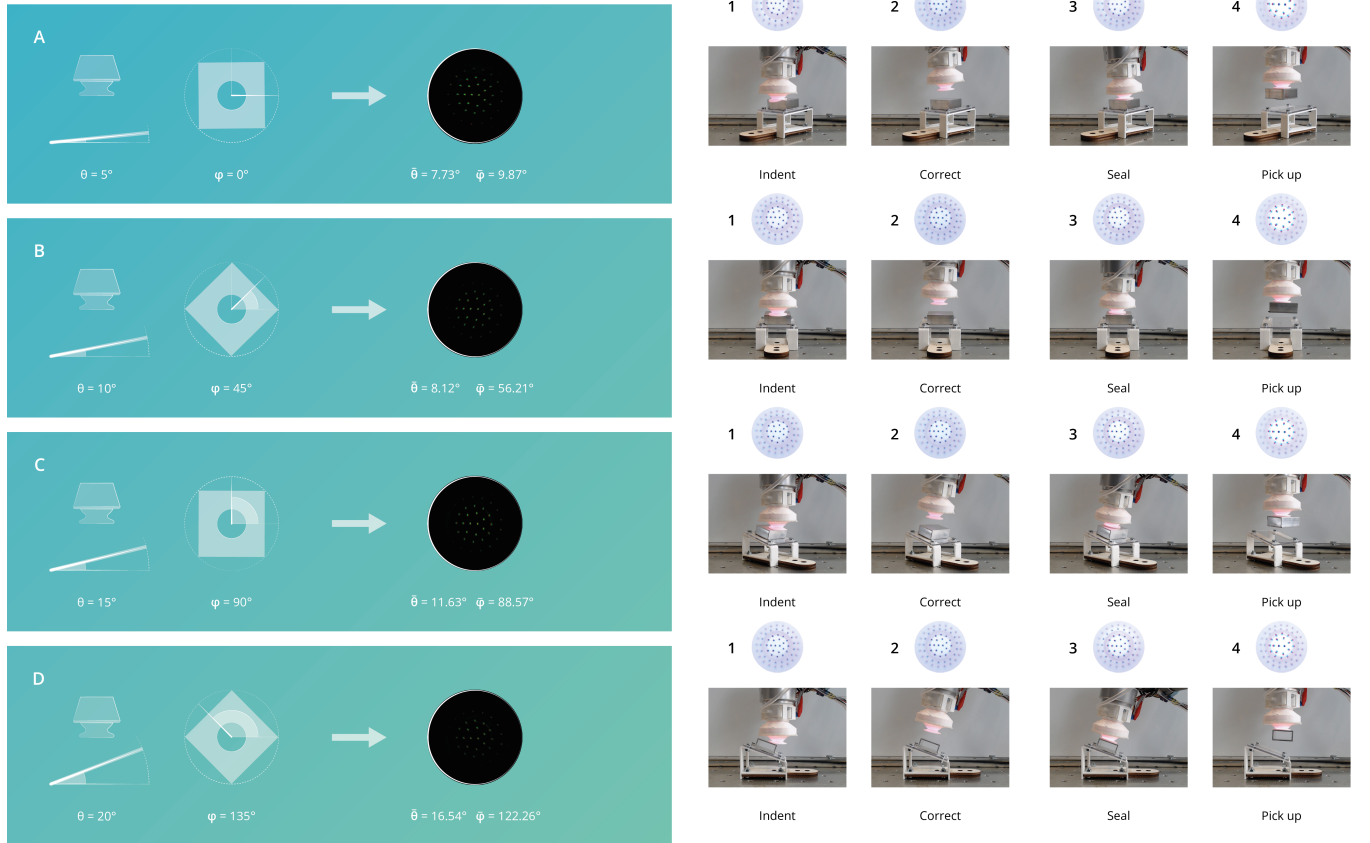


Fig. A19: Performance of Convolutional Neural Network when using it for live correction of orientation. For (A) a latitude (θ) of 5° and a longitude (ϕ) of 0° , (B) a latitude (θ) of 10° and a longitude (ϕ) of 45° , (C) a latitude (θ) of 15° and a longitude (ϕ) of 90° , (D) a latitude (θ) of 20° and a longitude (ϕ) of 135° . The left portion of each sub-figure shows the obtained difference image and predicted values. The right portion shows the front view and tactile images in the (1) 'indented' stage, (2) 'corrected' stage, (3) 'sealed' stage and (4) 'picked up' stage.

APPENDIX VII

DESIGN OPPORTUNITIES

The first category of design opportunities relates to the Polyjet printer resins. The rigid marker materials (VeroCyan-V and VeroMagenta-V) decrease the membranes' deformation abilities. The color change due to normal deformations in the membranes is then only caused by the decreasing distance between the two color filters, rather than also being dependent on the change in their size by elastic deformation. It is therefore highly recommended to explore the availability of stretchable photopolymers for the Polyjet printers. Additionally, substituting the Plasti-Dip coating with a white, stretchable resin would streamline post-processing procedures.

Regarding the flexible resin, Agilus30Clear, highly viscoelastic behavior can be observed. This may lead to hysteresis behavior and unwanted variations in the tactile images over time. To address this, it is recommended to explore the development of deformable, transparent resins that exhibit more purely elastic properties. Besides maintaining consistency in the tactile images, this would also enable speeding up control behavior in turbid environments. In the two most recent versions of the Chromatouch sensor, this problem was partly overcome by casting a transparent silicon layer between the two marker membranes [10], [11]. However, this hemispherical sensor shape led to a rather simple mold architecture for this post-processing step. Repeating this strategy for this work's design would prove rather complex and time-consuming. Another reason to choose different materials over Agilus30Clear is the fact that the hydrophilic nature of this material causes it to lose its transparency when submitted in water, which is crucial for the markers in the acetabular wall to be visible in the tactile images. This material property limits its use in wet environments.

Regarding the desired properties of the infundibular surface, a design conflict emerges. On the one hand, the infundibulum should be soft, thin, and highly conformable to effectively conform to various object shapes and ensure a secure seal. On the other hand, a stiffer and thick design is favorable to efficiently transfer the deformations to the parts containing the markers without loss of information. A similar conflict arises in the design of the acetabular wall. While it should exhibit compliance to capture meaningful tactile images with a high SNR, it must also possess the strength to withstand the low pressures and prevent collapse. Optimizing these trade-offs requires further analysis to determine the most effective configurations. Here, the parametric design functionalities of Rhino Grasshopper could be put to use to quickly explore and test several variants. An interesting solution described in van Veggel et al. (Appendix VIII-A), and implemented in several state-of-the-art designs [4], [20], [21], [22], is the application of a gradient stiffness design ranging from the infundibulum and acetabulum, resulting in a soft, conformable infundibulum that slightly transitions into a rigid acetabulum. Given the possibility of the Polyjet printing process to print multiple materials simultaneously, this design opportunity is worth exploring.

Continuing on the architecture of the infundibular surface, many state-of-the-art suction cups make use of additional surface features to improve adhesion on curved, rough and irregular surfaces (see Literature review in Appendix VIII-A). For example, addition of radial or circumferential grooves, application of microdenticles or using a wet adhesion layer in between the suction cup and the substrate. With the great geometrical flexibility of the Polyjet Printing process, these options could also be interesting for future versions of this work's design.

A final design opportunity worth exploring is the investigation of a geometry that induces bistability in the acetabular roof. This could enable the suction cup to maintain the acetabular roof's inflated or deflated state only requiring a negative or positive pressure pulse, rather than continuous actuation. This would save a significant amount of energy.

APPENDIX VIII

FILE PACKAGES

This Appendix lists Onedrive links to .zip file packages that were used throughout the design and experimental procedures. This includes the Literature review, files used for the modelling and manufacturing processes and python code for conduction of experiments and training of the Convolutional Neural Network.

A. Literature Research

Includes a pdf file of the Literature Review, and another pdf containing the supplementary materials. This review describes the state of the art in artificial suction cups. The obtained insights were used for the design of this work's suction cup.

<https://1drv.ms/u/s!AgSBRgdWjNn9jKkK34SXbCIEVxC5Hw?e=0c5yps>

B. Solidworks Files

Includes the Solidworks parts and assemblies of the mount. This was used to attach the suction cup to the UR5 Robot Arm. These parts were FDM 3D-printed with PLA.

<https://1drv.ms/u/s!AgSBRgdWjNn9jKRolkWQ31avuZSaRw?e=1o5671>

C. Grasshopper Files

Includes a file of print version A and B (no stiffness gradient) and a file of print version C (stiffness gradient design with VoxelPrinting Plugin). The sliders can be used to manually tweak 32 variable parameters.

<https://1drv.ms/u/s!AgSBRgdWjNn9jKRndf60N3zfi0R8MA?e=DP0S5w>

D. Experiment Code Files

Includes code used for conducting the pull-off tests, pickup tests, data collection process for training the CNN and code for the live correction demonstration with the trained CNN.

<https://1drv.ms/u/s!AgSBRgdWjNn9jKRl8AmzEf7jXQXjXA?e=he7YW1>

E. Raw Force and Pressure Data

Includes the raw force data for the normal pull-off tests and shear pull-off tests, as well as pressure data for both the pull-off tests and the object pickup tests.

<https://1drv.ms/u/s!AgSBRgdWjNn9jKRmcrDQFJZMkuWtPA?e=rRohPl>

F. Network Training Files

Includes CNN files for two prototypes. The first prototype matches the plots in the report. The second prototype was used for the demonstration. The folder for each prototype contains the labelled difference images used as training data, numpy arrays containing the extracted orientation and indentation labels, the downsampled RGBA pixel data of the images, a folder with the trained Convolutional Neural Network made with Tensorflow and a TFLite version of the network to be able to import it into the Raspberry Pi environment. It also includes a python file for training the CNN and visualize the data.

<https://1drv.ms/u/s!AgSBRgdWjNn9jKRp3ufnf7oFFM1iqA?e=L1IOy4>

APPENDIX IX

VIDEO LINKS

This Appendix lists the Google Photos links to the videos that were listed in the report. These include pull-off and pickup test videos, the explanation of the data collection process, and videos of the suction cup correcting for orientation errors.

A. Pull-off Tests

Below, you can find the links to the normal pull-off test and the shear pull-off test with both a front view and inside (marker-image) view. The force and pressure data is plotted live on the left side of the screen.

<https://photos.app.goo.gl/91A5VaBnzBJvPDM38> (Normal pull-off)

<https://photos.app.goo.gl/srrfLVXafQWnbzRR7> (Shear pull-off)

B. Pickup Tests

Below is the album link to the three object pickup tests. These include a video of picking up an aluminum block, beam and cylinder. All videos show both the front view and the inside (marker-image) view. Pressure data is plotted live on the left side of the screen.

<https://photos.app.goo.gl/cmHHiHpNHFyvSFux5>

C. Data Collection

Includes a video of randomized orientations with a front view and inside (marker-image) view. The second video shows how the training data is collected, post-processed and labelled.

<https://photos.app.goo.gl/xiSvldYu7aAD7hyR7> (Randomized orientations)

<https://photos.app.goo.gl/UstuQzxsUJvUuwJ47> (Data collection & post-processing)

D. Passive Correction

This link refers to a video of the suction cup picking up an object that is oriented according to the prediction errors of the Convolutional Neural Network. This shows that the passive compliance of the suction cup is sufficient to correct for these error orders.

<https://photos.app.goo.gl/ShdfCq25gmWTnEiz8>

E. Active Correction

The link below refers to the album containing four pickup videos. Each video presents an object in a different orientation. Pickup tests are conducted where the trained Convolutional Neural Network is used for correcting the orientation errors and sealing on the object perpendicularly.

<https://photos.app.goo.gl/9rsUGF3uUYmkVB5d8>